The Astrophysical Journal, 883:111 (17pp), 2019 October 1 https://doi.org/10.3847/1538-4357/ab3c66

Discovery and Early Evolution of ASASSN-19bt, the First TDE Detected by *TESS*

Thomas W.-S. Holoien[1,18], Patrick J. Vallely[2,19], Katie Auchettl[3], K. Z. Stanek[2,4], Christopher S. Kochanek[2,4,20], K. Decker French[1,21], Jose L. Prieto[5,6], Benjamin J. Shappee[7], Jonathan S. Brown[8], Michael M. Fausnaugh[9], Subo Dong[10], Todd A. Thompson[2,4,11], Subhash Bose[10], Jack M. M. Neustadt[2], P. Cacella[12], J. Brimacombe[13], Malhar R. Kendurkar[14], Rachael L. Beaton[1,15,21,22], Konstantina Boutsia[16], Laura Chomiuk[17], Thomas Connor[1], Nidia Morrell[16], Andrew B. Newman[1], Gwen C. Rudie[1], Laura Shishkovksy[17], and Jay Strader[17]

[1] The Observatories of the Carnegie Institution for Science, 813 Santa Barbara Street, Pasadena, CA 91101, USA; tholoien@carnegiescience.edu
[2] Department of Astronomy, The Ohio State University, 140 West 18th Avenue, Columbus, OH 43210, USA
[3] DARK, Niels Bohr Institute, University of Copenhagen, Lyngbyvej 2, DK-2100 Copenhagen, Denmark
[4] Center for Cosmology and AstroParticle Physics (CCAPP), The Ohio State University, 191 W. Woodruff Avenue, Columbus, OH 43210, USA
[5] Núcleo de Astronomía de la Facultad de Ingeniería y Ciencias, Universidad Diego Portales, Av. Ejército 441, Santiago, Chile
[6] Millennium Institute of Astrophysics, Santiago, Chile
[7] Institute for Astronomy, University of Hawai'i, 2680 Woodlawn Drive, Honolulu, HI 96822, USA
[8] Department of Astronomy and Astrophysics, University of California, Santa Cruz, CA 95064, USA
[9] Department of Physics and Kavli Institute for Astrophysics and Space Research, Massachusetts Institute of Technology, Cambridge, MA 02139, USA
[10] Kavli Institute for Astronomy and Astrophysics, Peking University, Yi He Yuan Road 5, Hai Dian District, Beijing 100871, People's Republic of China
[11] Institute for Advanced Study, 1 Einstein Drive, Princeton, NJ 08540, USA
[12] DogsHeaven Observatory, SMPW Q25 CJ1 LT10B, Brasilia, DF 71745-501, Brazil
[13] Coral Towers Observatory, Cairns, Queensland 4870, Australia
[14] Prince George Astronomical Observatory, 7765 Tedford Road, Prince George, British Columbia, V2N 6S2, Canada
[15] Department of Astrophysical Sciences, Princeton University, 4 Ivy Lane, Princeton, NJ 08544, USA
[16] Las Campanas Observatory, Carnegie Observatories, Casilla 601, La Serena, Chile
[17] Center for Data Intensive and Time Domain Astronomy, Department of Physics and Astronomy, Michigan State University, East Lansing, MI 48824, USA
Received 2019 April 26; revised 2019 August 2; accepted 2019 August 2; published 2019 September 26

Abstract

We present the discovery and early evolution of ASASSN-19bt, a tidal disruption event (TDE) discovered by the All-Sky Automated Survey for Supernovae (ASAS-SN) at a distance of $d \simeq 115$ Mpc and the first TDE to be detected by *TESS*. As the TDE is located in the *TESS* Continuous Viewing Zone, our data set includes 30 minute cadence observations starting on 2018 July 25, and we precisely measure that the TDE begins to brighten ~8.3 days before its discovery. Our data set also includes 18 epochs of *Swift* UVOT and XRT observations, 2 epochs of *XMM-Newton* observations, 13 spectroscopic observations, and ground data from the Las Cumbres Observatory telescope network, spanning from 32 days before peak through 37 days after peak. ASASSN-19bt thus has the most detailed pre-peak data set for any TDE. The *TESS* light curve indicates that the transient began to brighten on 2019 January 21.6 and that for the first 15 days, its rise was consistent with a flux $\propto t^2$ power-law model. The optical/UV emission is well fit by a blackbody spectral energy distribution, and ASASSN-19bt exhibits an early spike in its luminosity and temperature roughly 32 rest-frame days before peak and spanning up to 14 days, which has not been seen in other TDEs, possibly because UV observations were not triggered early enough to detect it. It peaked on 2019 March 4.9 at a luminosity of $L \simeq 1.3 \times 10^{44}$ erg s^{-1} and radiated $E \simeq 3.2 \times 10^{50}$ erg during the 41 day rise to peak. X-ray observations after peak indicate a softening of the hard X-ray emission prior to peak, reminiscent of the hard/soft states in X-ray binaries.

Key words: accretion, accretion disks – black hole physics – galaxies: nuclei

Supporting material: data behind figure, machine-readable table

1. Introduction

Tidal disruption events (TDEs) are rare transient phenomena that occur when a star passes within the tidal radius of a supermassive black hole (SMBH). This results in the tidal forces from the SMBH overwhelming the self-gravity of the star, tearing the star apart. In the classical picture, roughly half of the disrupted stellar material is ejected from the system while the rest remains bound to the SMBH and falls back to pericenter at a rate asymptotically proportional to $t^{-5/3}$. A portion of this material then forms an accretion disk, producing a luminous, short-lived flare (e.g., Lacy et al. 1982; Rees 1988; Evans & Kochanek 1989; Phinney 1989).

The initial theoretical work (e.g., Lacy et al. 1982; Rees 1988; Evans & Kochanek 1989; Phinney 1989) predicted temperatures of $T \sim$ a few $\times 10^5$ K, which would result in emission peaking at soft X-ray energies, and that the transient luminosity would follow the same $t^{-5/3}$ time dependence as the mass fallback rate. In recent years, however, wide-area sky surveys have discovered an increasing number of TDE candidates that exhibit a large range of observational properties that differ from the classical picture (e.g., van Velzen et al. 2011; Cenko et al. 2012a; Gezari et al. 2012, 2017, 2015; Arcavi et al. 2014; Chornock et al. 2014; Holoien et al. 2014; Vinkó et al. 2015; Brown et al. 2016, 2017, 2018; Holoien et al. 2016a, 2016b, 2018, 2019b; Auchettl et al. 2017; Blagorodnova et al. 2017; Leloudas et al. 2019; van Velzen et al. 2019). These objects typically exhibit nearly

[18] Carnegie Fellow.
[19] NSF Graduate Fellow.
[20] Radcliffe Fellow.
[21] Hubble Fellow.
[22] Carnegie-Princeton Fellow.

constant temperatures roughly an order of magnitude cooler than the initial predictions, peaking at ultraviolet (UV) wavelengths, a wide range of luminosity decline rates that vary over time, and broad hydrogen and helium emission lines of varying relative strength in their optical spectra. Despite significant theoretical work on these objects, a single, unifying model has yet to be developed that can explain all of the observations. However, it is now clear that TDE emission depends on a range of factors, including the properties of the disrupted star (e.g., MacLeod et al. 2012; Kochanek 2016), the evolution of the stellar debris stream after disruption (e.g., Kochanek 1994; Strubbe & Quataert 2009; Guillochon & Ramirez-Ruiz 2013; Hayasaki et al. 2013, 2016; Piran et al. 2015; Shiokawa et al. 2015), and radiative transfer effects (e.g., Gaskell & Rojas Lobos 2014; Strubbe & Murray 2015; Roth et al. 2016; Roth & Kasen 2018).

Only a small subset of TDEs has been discovered prior to peak light, making it difficult to study the evolution of the stellar debris following disruption and the formation of the accretion disk, and resulting in a significant gap in our theoretical understanding of these objects. Only in recent years have early discoveries become more common, as sky surveys with high cadence and wide coverage, such as the All-Sky Automated Survey for Supernovae (ASAS-SN; Shappee et al. 2014; Kochanek et al. 2017), the Palomar Transient Factory (PTF; Law et al. 2009), the Asteroid Terrestrial-impact Last Alert System (ATLAS; Tonry et al. 2018), and the Zwicky Transient Facility (ZTF; Bellm et al. 2019), have grown and come online. This has resulted in a growing sample of TDEs with several weeks of observations prior to peak (e.g., Holoien et al. 2018; Leloudas et al. 2019; van Velzen et al. 2019; Wevers et al. 2019), but there has yet to be a case where the transient has been caught within hours of beginning to brighten, as has been done with several supernovae (SNe).

The *Kepler* spacecraft, which continuously monitored thousands of galaxies between its original four-year primary mission and the *K2* Campaign 16 Supernova Experiment, created a new paradigm for early-time SN light curves, as it obtained light curves of six SNe spanning from prior to explosion through the early rise at extremely high cadence. The *Kepler* sample includes ASASSN-18bt, which has the most precisely measured SN light curve to date (Olling et al. 2015; Garnavich et al. 2016; Dimitriadis et al. 2019; Shappee et al. 2019).

The *Transiting Exoplanet Survey Satellite* (*TESS*; Ricker et al. 2015) has the potential to do the same for TDEs, as it combines continuous space-based monitoring for time spans ranging from one month to one year with an extremely wide field of view, providing both the ability to observe TDEs minutes after they start to brighten and the sky coverage needed to have any likelihood of observing a TDE. *TESS* has already detected significantly more SNe than *Kepler* in less than a year of operation (Fausnaugh et al. 2019; Vallely et al. 2019), and it can achieve a 3σ limiting magnitude of $\sim$20 mag in 8 hr of observation, making it an ideal complement to modern high-cadence ground-based surveys.

Here, we present the discovery and early-time observations of ASASSN-19bt, a TDE discovered by ASAS-SN on 2019 January 29 in the galaxy 2MASX J07001137−6602251. ASASSN-19bt is located in the *TESS* Continuous Viewing Zone (CVZ) and is the first TDE flare detected by *TESS*, providing us with an unprecedented cadence on its rising light curve and the ability to precisely measure the time when the transient began to brighten. At a redshift of $z = 0.0262$ ($d = 115.2$ Mpc for $H_0 = 69.6\,\mathrm{km\,s^{-1}\,Mpc^{-1}}$, $\Omega_M = 0.29$, and $\Omega_\Lambda = 0.71$) based on an archival 6 dF spectrum obtained from NED (Jones et al. 2009), it is also one of the nearest TDEs discovered to date, and it had a peak UV magnitude comparable to that of ASASSN-14li (Holoien et al. 2016b). In Section 2, we describe the discovery of ASASSN-19bt, the available archival data for the host, and the observations obtained in our follow-up campaign. In Section 3, we fit the physical properties of the TDE using the early light curves, describe the transient's blackbody evolution and compare it to other TDEs in the literature, and analyze the early spectroscopic evolution of ASASSN-19bt. Finally, a summary of our results and a discussion of the physical implications are given in Section 4.

2. Discovery and Observations

ASAS-SN is an ongoing project designed to monitor the entire visible sky in an unbiased way with a rapid cadence to discover bright, nearby transients. To accomplish this, we use units hosted by the Las Cumbres Observatory global telescope network (Brown et al. 2013) at multiple sites around the globe, each consisting of four 14 cm telescopes on a common mount. ASAS-SN expanded in 2017 and currently operates with five units, located in Hawaii, Texas, Chile, and South Africa. ASAS-SN can observe the entire visible sky to a depth of $g \sim 18.5$ mag roughly once every 24 hr, weather permitting (Shappee et al. 2014; Kochanek et al. 2017). In order to maximize the synergy between ASAS-SN and *TESS*, ASAS-SN monitors the *TESS* fields at an increased cadence, allowing us to discover transients in the *TESS* fields and trigger follow-up data collection as soon as possible in order to complement the *TESS* light curve.

ASASSN-19bt was discovered on 2019 January 29.91 at R.A. = 07:00:11.41, decl. = −66:02:25.16 (J2000) in *g*-band images obtained from the ASAS-SN "Payne-Gaposchkin" unit located in Sutherland, South Africa, and we promptly announced its discovery to the community via the Transient Name Server, which assigned it the designation AT 2019ahk.[23] Because its position was consistent with the nucleus of its host galaxy and it was located in a field that was part of the *TESS* CVZ, we triggered a spectroscopic follow-up observation with the Low-dispersion Survey Spectrograph 3 (LDSS-3) mounted on the *Magellan* Clay 6.5 m telescope on 2019 January 31.20. The spectrum revealed a strong blue continuum, narrow emission features consistent with those in an archival spectrum of the host (see Section 2.1), and no obvious broad emission features. Based on this, we publicly announced the discovery and classification of the target as a possible young TDE (Cacella et al. 2019), noting that a lack of broad hydrogen and helium emission lines prior to peak light has been seen in other TDEs (e.g., Holoien et al. 2018). Figure 1 shows images of ASASSN-19bt taken near peak light from *TESS*, ASAS-SN, and the Las Cumbres Observatory 1 m telescopes. Despite the large pixel sizes of ASAS-SN and *TESS*, the transient is clearly detected by both instruments.

Based on the preliminary classification, we requested and were awarded target-of-opportunity (TOO) observations from the *Neil Gehrels Swift Gamma-ray Burst Mission* (*Swift*; Gehrels et al. 2004), UltraViolet and Optical Telescope

[23] https://wis-tns.weizmann.ac.il/object/2019ahk

Figure 1. Images of ASASSN-19bt near peak light obtained with ASAS-SN (left panel), *TESS* (center panel), and a Las Cumbres Observatory 1 m telescope (right panel). The red circle has a radius of 5.″0 and is centered on the position of the transient.

(UVOT; Roming et al. 2005), and X-ray Telescope (XRT; Burrows et al. 2005). The *Swift* observations confirmed that the transient was UV-bright and exhibited very faint X-ray emission, both consistent with the TDE classification, and we began a multiwavelength follow-up campaign to observe the transient.

2.1. Archival Data of 2MASX J07001137−6602251

We obtained *BVgri* magnitudes of the host galaxy from the AAVSO Photometric All-Sky Survey Data Release 10 (APASS; Henden et al. 2015), JHK_S magnitudes from the Two Micron All-Sky Survey (2MASS), and *W*1 and *W*2 measurements from the *Wide-field Infrared Survey Explorer* (*WISE*; Wright et al. 2010) AllWISE data release. 2MASX J07001137−6602251 is at a decl. too far south to be observed by optical surveys such as the Sloan Digital Sky Survey (SDSS) and Pan-STARRS or radio surveys like FIRST and NVSS. It is not detected in archival data from, or was not previously observed by, *Spitzer*, *Herschel*, or the *Hubble Space Telescope* (*HST*).

Serendipitously, 2MASX J07001137−6602251 is located approximately 8.′5 away from the BL Lac-type object PKS 0700−661, which was observed several times by *Swift* in 2009, 2010, 2014 and 2018 (target IDs 38456, 41619, and 83377). Due to the 17.′0 × 17.′0 field of view of *Swift*, 2MASX J07001137−6602251 was captured in several of these archival observations. While it is located at the edge of the field, making it difficult to use these archival images as image subtraction templates, we obtained archival *Swift* UVOT magnitudes by first summing all of the available data in each of the six UVOT filters using the HEAsoft software task `uvotimsum`, and then extracting counts from the combined images in a 5.″0 radius aperture using the software task `uvotsource`, with a sky aperture of ∼40.″0 radius to estimate and subtract the background counts. We converted the archival count rates to magnitudes and fluxes using the most recent UVOT calibration (Poole et al. 2008; Breeveld et al. 2010). The *Swift* UVOT, APASS, 2MASS, and *WISE* magnitudes of the host that we used to fit the host galaxy spectral energy distribution (SED) and estimate the host flux (see below) are shown in Table 1.

There were pre-event X-ray observations of 2MASX J07001137−6602251 by the *ROSAT* All-Sky Survey (Voges et al. 1999) circa 1990 and in the serendipitous *Swift* X-Ray Telescope (XRT; Burrows et al. 2005) observations. No source was detected by *ROSAT* to a 3σ upper limit of 4.7×10^{-3} counts s^{-1} in the 0.3–2.0 keV range. Assuming a $\Gamma = 1.75$ power-law spectrum typical of an active galactic nucleus (AGN; e.g., Ricci et al. 2017) and an H I column density of 7.1×10^{20} cm^{-2}, we derive a 3σ absorbed flux upper limit of $\sim 1.7 \times 10^{-12}$ erg cm^{-2} s^{-1} over the 0.3–10.0 keV energy range. This corresponds to an absorbed luminosity of 2.7×10^{42} erg s^{-1}, implying that the host does not harbor a strong AGN (e.g., Ricci et al. 2017). Interestingly, we detect weak (∼3σ) X-ray emission from the first *Swift* observation (ID 38450) in 2009, but a follow-up observation (also ID 38450) taken ∼20 days later does not show any significant X-ray emission. Further observations (IDs 41619 and 83377) taken in 2010, 2014 and 2018 show no evidence of X-ray emission.

The detection in the first *Swift* observation has a count rate of $(2.3 \pm 1) \times 10^{-3}$ counts/sec in the 0.3–10.0 keV energy range. Assuming the same model we used to derive the *ROSAT* upper

Table 1
Archival Host Photometry

Filter	Magnitude	Magnitude Uncertainty
*UVW*2	19.55	0.06
*UVM*2	19.59	0.07
*UVW*1	19.08	0.06
$U_{\rm UVOT}$	18.10	0.04
B_J	16.69	0.05
g	16.38	0.06
V_J	15.98	0.01
r	15.73	0.06
i	15.30	0.10
J	14.55	0.05
H	14.26	0.06
K_S	14.47	0.11
*W*1	15.33	0.02
*W*2	16.00	0.02

Note. Archival magnitudes of 2MASX J07001137−6602251 from *Swift* (UV+*U*), APASS (*BgVri*), 2MASS (JHK_S), and *WISE* (*W*1, *W*2) used as inputs for host SED fitting with FAST. Magnitudes in the *Swift* filters are 5.″0 aperture magnitudes measured from archival data, while APASS, 2MASS, and *WISE* magnitudes were taken from their respective catalogs. The *Swift* and APASS magnitudes shown here were also used to calculate the host's flux in the UV and optical bands to use for host subtraction from our follow-up photometry (see Sections 2.4 and 2.5). All magnitudes are in the AB system.

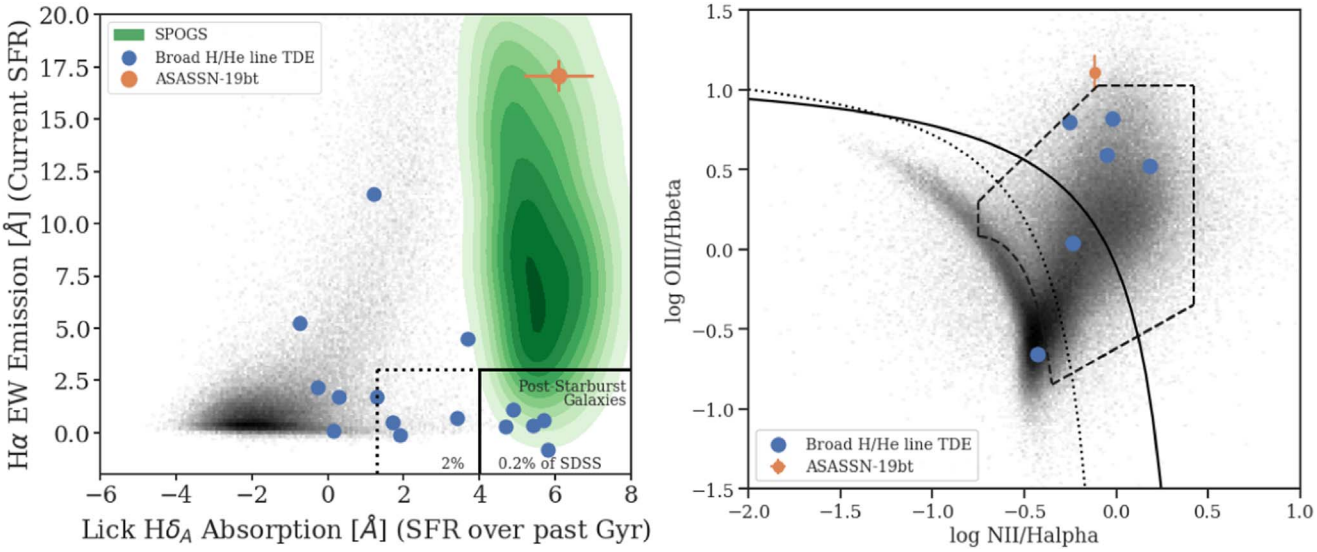

Figure 2. Left panel: lick $H\delta_A$ absorption (tracing star formation over the last Gyr) compared to the $H\alpha$ EW emission (usually tracing current star formation) for 2MASX J07001137−6602251 in orange and several other TDE hosts in blue. Galaxies from the SDSS main spectroscopic survey (Strauss et al. 2002) are shown in gray. The green contours show the population of shocked post-starburst (SPOG) galaxies (Alatalo et al. 2016). 2MASX J07001137−6602251 has strong $H\alpha$ emission like many star-forming galaxies, but its strong Balmer absorption places it closer to the population of SPOGs. Right panel: BPT diagram showing 2MASX J07001137−6602251 (orange) and other TDE host galaxies (blue). Galaxies from the SDSS main spectroscopic survey (Strauss et al. 2002) are shown in gray. The solid line is the theoretical maximum starburst line from Kewley et al. (2001), and the dotted line is the observed starburst−AGN separation from Kauffmann et al. (2003). The region enclosed by the dashed lines indicates galaxies with line ratios consistent with shocks. 2MASX J07001137−6602251 is in the Seyfert or non-star-forming portion of this diagram but slightly outside of the shocked region, so it is similar to, but not a part of, the SPOG population.

limit, this corresponds to a flux of $(9.6 \pm 4) \times 10^{-14}$ erg cm^{-2} s^{-1} and a luminosity of $(1.5 \pm 0.7) \times 10^{41}$ erg s^{-1} in the 0.3–10.0 keV energy range. This emission could be indicative of a weak AGN, but there are too few counts to determine the origin of the emission.

If we then combine all of the *Swift* non-detections, we obtain a 3σ upper limit on the count rate of 9.7×10^{-4}, which corresponds to a flux limit of 4.1×10^{-14} erg cm^{-2} s^{-1} and a luminosity limit of 6.3×10^{40} erg s^{-1}. For our black hole (BH) mass estimate (see below), the apparent detection corresponds to 2×10^{-4} of the Eddington luminosity given our estimated BH mass, and the upper limit from the *Swift* non-detections is two times lower.

We assessed the recent star-formation history by measuring the $H\alpha$ equivalent width (EW) and Lick $H\delta_A$ index of the 6 dF spectrum as in French et al. (2016), finding that the $H\alpha$ EW is 17.11 ± 0.76 Å and the Lick $H\delta_A$ index is 6.08 ± 0.92 Å, where we are defining positive values of EW as emission. The left panel of Figure 2 shows the $H\alpha$ EW compared to the Lick $H\delta_A$ index for 2MASX J07001137−6602251 and several other TDE host galaxies. While its Lick $H\delta_A$ index is similar to those of other TDE hosts, 2MASX J07001137−6602251 exhibits a significantly stronger $H\alpha$ emission feature. We also measured the N II6584/$H\alpha$ and O III5007/$H\beta$ line ratios in order to analyze the galaxy using the BPT diagram (Baldwin et al. 1981) shown in the right panel of Figure 2. The N II6584/$H\alpha$ flux ratio is 0.76 ± 0.03, and the O III5007/$H\beta$ flux ratio is 12.85 ± 3.36. These line ratios indicate the possible presence of a Seyfert in the host galaxy but could also be generated by shocks (e.g., Rich et al. 2015).

As can be seen in the left panel of Figure 2, 2MASX J07001137-6602251 is similar to the "shocked post-starburst" (SPOG) galaxies identified by Alatalo et al. (2016). SPOGs combine strong Balmer absorption with emission line ratios consistent with shocks and inconsistent with star formation. This selection differs from an E+A or K+A selection by allowing for $H\alpha$ emission, even if much of the emission is unlikely to be from star formation. Most SPOGs have star-formation histories similar to traditionally selected post-starburst galaxies, yet are on average younger and thus may have higher dust obscuration (French et al. 2018). There are several theoretical predictions for a higher TDE rate in young starburst/post-starburst galaxies (Madigan et al. 2018; Stone et al. 2018), which would predict an intrinsically high TDE rate in SPOGs as well, although the observed rate might be lower due to the extra dust.

The right panel of Figure 2 shows a BPT diagram of 2MASX J07001137−6602251 and several other TDE hosts along with a comparison sample from the SDSS main spectroscopic survey (Strauss et al. 2002). The host of ASASSN-19bt lies in the Seyfert or non-star-forming portion of the diagram, along with several other TDE hosts, but it lies outside the region enclosing galaxies with line ratios consistent with shocks. Thus, while it is similar in many ways to SPOGS, it is likely not a member of this population.

We fit the SED of the host galaxy using the Fitting and Assessment of Synthetic Templates (FAST; Kriek et al. 2009) code. We used the *Swift* UVOT UV and *U*, APASS *BVgri*, 2MASS JHK_S, and *WISE* *W*1 and *W*2 magnitudes given in Table 1 to constrain the model. We assumed a Cardelli et al. (1989) extinction law with $R_V = 3.1$, a Galactic extinction of $A_V = 0.336$ mag (Schlafly & Finkbeiner 2011), a Salpeter initial mass function, an exponentially declining star-formation history, and stellar population models from Bruzual & Charlot (2003) for the fit. The FAST fit indicates that 2MASX J07001137−6602251 has a stellar mass of $M_\star = 1.1^{+1.3}_{-0.1} \times 10^{10}\,M_\odot$, an age of $3.2^{+5.8}_{-0.1}$ Gyr, and a star-formation rate of SFR $= 1.7^{+0.6}_{-0.1} \times 10^{-1}\,M_\odot\,\mathrm{yr}^{-1}$. Using the average stellar-mass-to-bulge-mass ratio from the hosts of ASASSN-14ae, ASASSN-14li, and ASASSN-15oi (Holoien et al. 2014, 2016a, 2016b) to scale the stellar mass of the host, as we have done

Table 2
Host-subtracted Photometry of ASASSN-19bt

MJD	Filter	Magnitude	Telescope/Observatory
58491.66	*TESS*	>18.84	*TESS*
58491.74	*TESS*	>20.48	*TESS*
58491.82	*TESS*	>19.10	*TESS*
…			
58578.42	*UVW2*	15.72 ± 0.05	*Swift*
58581.62	*UVW2*	15.87 ± 0.05	*Swift*
58584.15	*UVW2*	15.90 ± 0.07	*Swift*

Note. Host-subtracted magnitudes and 3σ upper limits for all photometric follow-up data. The Telescope/Observatory column indicates the source of the data for each epoch: "ASAS-SN" is used for ASAS-SN survey data, "*TESS*" is used for *TESS* data, "LCOGT_1m" is used for data from the Las Cumbres Observatory 1 m telescopes, and "*Swift*" is used for *Swift* UVOT data. A range of dates given in column 1 indicates the dates of the earliest and latest observations in a set that were combined to improve the signal-to-noise. All measurements have been corrected for Galactic extinction and are presented in the AB system. *TESS* data has been binned in 2 hr bins, as described in Section 2.3, with the MJD at the center of the bin given in Column 1.

(This table is available in its entirety in machine-readable form.)

with previous TDEs (e.g., Holoien et al. 2019b), results in an estimated bulge mass of $M_B \simeq 10^{9.4}\,M_\odot$. This corresponds to an estimated BH mass of $M_{\rm BH} = 10^{6.8}\,M_\odot$ (McConnell & Ma 2013), comparable to the BH mass estimates for other TDE hosts (e.g., Holoien et al. 2014, 2016a, 2016b; Brown et al. 2017; Wevers et al. 2017; Mockler et al. 2019).

2.2. ASAS-SN Light Curve

ASAS-SN images are processed in real time using a fully automated pipeline incorporating image subtraction that is performed with the ISIS package (Alard & Lupton 1998; Alard 2000). As ASAS-SN monitors the *TESS* fields with an increased cadence, the field containing ASASSN-19bt was observed on average 1–2 times per night before and after discovery of the transient with cameras in our "Cassius," "Paczynski," and "Payne-Gaposchkin" units, located in Chile and South Africa. To ensure that no transient flux was present in the reference images used for image subtraction, we constructed a reference image for each camera that observed ASASSN-19bt using only data obtained earlier than 2018 December 1, roughly 60 days prior to discovery. We used these references as templates to subtract the background and host emission from all data taken after 2019 January 1, ensuring that we capture the full rise of the TDE in ASAS-SN data.

We performed aperture photometry on each host-subtracted image using the IRAF `apphot` package and an aperture 3 pixels in radius (roughly equivalent to 21.″0). We calibrated the ASAS-SN *g*-band magnitudes using several stars near the transient with magnitudes available in APASS. For many pre-discovery epochs, when ASASSN-19bt was very faint or not detected, we combined images taken over several days on the same camera to improve the signal-to-noise of our detections and obtain deeper limits on the TDE emission. All ASAS-SN photometry, including both detections and 3σ upper limits, is presented in Table 2, and we show the ASAS-SN light curve in Figure 3 along with our follow-up photometry and photometry from *TESS*.

While SPOGs typically do have a higher amount of dust obscuration, and the host emission lines indicate that the

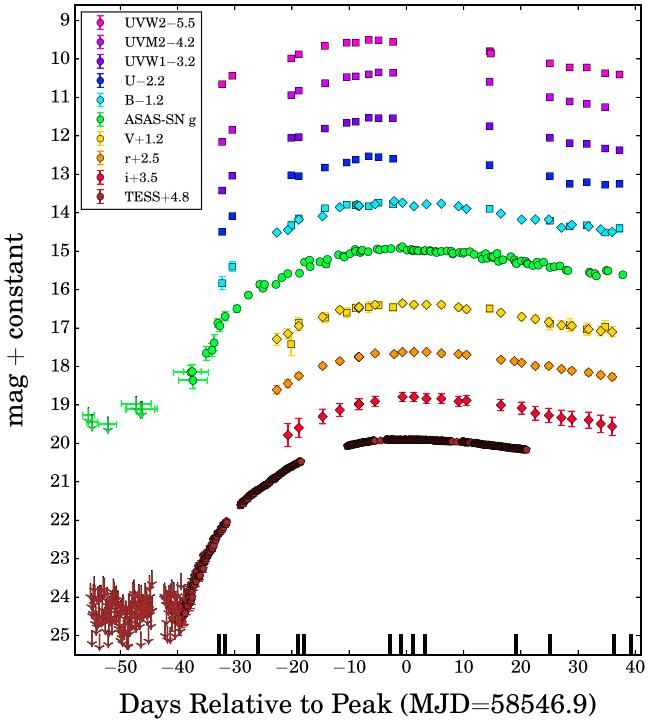

Figure 3. Host-subtracted UV and optical light curves of ASASSN-19bt, showing the ASAS-SN (*g*, circles), *Swift* (UV+*UBV*, squares), Las Cumbres Observatory 1 m telescopes (*BVri*, diamonds), and *TESS* (pentagons) photometry and spanning from roughly 60 days prior to peak brightness (MJD = 58,546.9) to 35 days after. Arrows indicate 3σ upper limits for epochs where no transient flux is detected. *Swift* UVOT *B* and *V* data were converted to Johnson *B* and *V* magnitudes to enable direct comparison with other data. Error bars on the time axis for pre-discovery ASAS-SN data indicate the date range of observations combined to obtain deeper limits and higher signal-to-noise detections. The *TESS* light curve shows the median magnitude of observations in 2 hr bins, with epochs with negative subtracted flux or prior to our inferred time of first light (MJD = 58,504.6, see Section 3.2) converted into 3σ upper limits. Black bars along the *X*-axis show epochs of spectroscopic follow-up. All data are corrected for Galactic extinction and are presented in the AB system.

emission line regions may have a higher amount of obscuration, our host SED fit is sufficiently good to not require additional dust correction. Furthermore, the fact that we clearly detect the TDE in UV filters, and the fact that TDE SED is well fit by a blackbody without any additional dust correction (see Figure 9) implies that any potential host extinction along the line of sight to the TDE must be minimal. For this reason, while we correct all of our photometry for Galactic extinction, we do not apply any host extinction correction to our measurements.

2.3. TESS *Observations*

Located in the *TESS* CVZ near the South Ecliptic Pole, ASASSN-19bt has been observed by *TESS* almost constantly since science operations commenced in late July of 2018. The location of the TDE fell within a chip gap during Sector 6 observations, but this is the only sector in Cycle 1 for which *TESS* did not observe it. There are five full sectors of pre-disruption observations and a full orbit's worth of observations obtained in Sector 7 prior to first light from the TDE. After first light, the transient's rise is continuously sampled by *TESS* throughout the remainder of Sector 7 and all of Sector 8, with the exception of a gap in Sector 8 caused by an instrument anomaly on the spacecraft. The transient's epoch of maximum

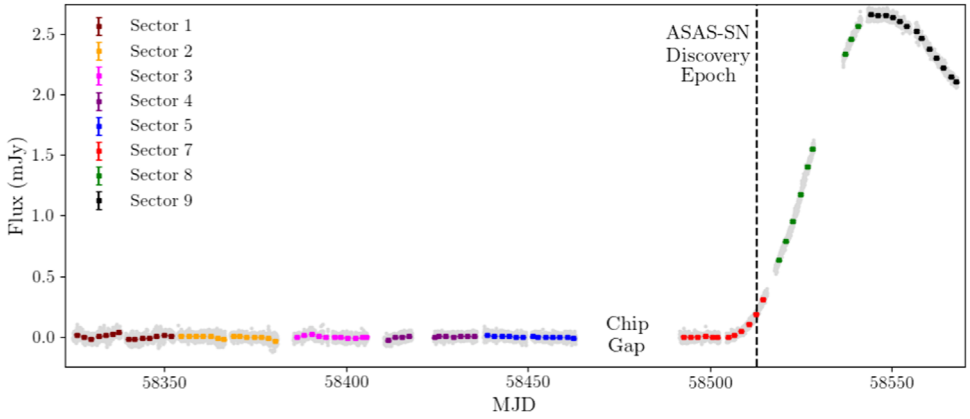

Figure 4. The *TESS* image subtraction light curve of ASASSN-19bt obtained for all currently available *TESS* sectors. ASASSN-19bt was not observed in *TESS* Sector 6 as the transient coordinates fell on a *TESS* chip gap. The extended gap in Sector 8 observations is due to an instrument anomaly on the spacecraft. Flux values for every epoch are shown in light gray, and the colored points show the mean values of 2 day bins. Error bars are shown for all of the colored points but are considerably smaller than the symbols.

brightness and initial decline are captured in the Sector 9 observations.

As with the ASAS-SN data, we used the ISIS package (Alard & Lupton 1998; Alard 2000) to perform image subtraction on the *TESS* full-frame images (FFIs) to produce high-fidelity light curves. Due to the large pixel scale of the *TESS* observations, we elected not to rotate a single reference image for use across various sectors and instead chose to construct independent reference images for each sector. This was achieved by selecting the first 100 FFIs of good quality obtained during that sector, excluding those with sky background levels or PSF widths above average for the sector. We entirely exclude any FFIs with data quality flags from our analysis. We adopted additional conservative quality cuts, excluding FFIs obtained when the spacecraft's pointing was compromised, when *TESS* was either impacted by or recovering from an instrument anomaly, or when significant background effects due to scattered light were present in the images.

Because a considerable amount of flux from the TDE is present in the images used to construct the Sector 8 reference, fluxes in the raw difference light curve for this sector are systematically lower than the intrinsic values. We correct for this by applying an offset, which we calculate by matching the first 12 hr of Sector 8 observations (24 epochs) to an extrapolation of the Sector 7 power-law fit shown in Figure 6 (see Section 3.2). We subsequently take a simple linear fit between the last 12 hr of Sector 8 observations and the first 12 hr of Sector 9 observations to calculate the offset for the Sector 9 light curve. The measured fluxes were converted into *TESS*-band magnitudes using an instrumental zero-point of 20.44 electrons per second in the FFIs, based on the values provided in the *TESS* Instrument Handbook (Vanderspek et al. 2018). *TESS* observes in a single broadband filter, spanning roughly 6000–10000 Å with an effective wavelength of ∼7500 Å, and *TESS* magnitudes are calibrated to the Vega system (Sullivan et al. 2015). The full, host-subtracted light curves for all currently available *TESS* sectors are shown in Figure 4.

For comparison with our other photometry, we binned the *TESS* data for epochs after MJD = 58,491 in 2 hr bins by taking the median flux in each bin and calculating the *TESS* magnitude from the median flux. We converted the *TESS* Vega magnitudes to the AB system using an offset of $m_{AB}-m_{\rm Vega} = 0.411$ to match our other photometry. *TESS* magnitudes and 3σ limits are presented in Table 2 and shown in Figure 3.

2.4. Swift *UVOT Observations*

Following our initial classification of ASASSN-19bt as a possible TDE, we requested and were awarded 17 epochs of TOO observations with the *Swift* UVOT and XRT, with the first epoch of observations obtained within 2 days of discovery.

UVOT observations were obtained in the *V* (5468 Å), *B* (4392 Å), *U* (3465 Å), *UVW*1 (2600 Å), *UVM*2 (2246 Å), and *UVW*2 (1928 Å) filters (Poole et al. 2008) in most epochs, with some epochs having only a subset of filters due to scheduling. Each epoch of UVOT data contains two observations in each filter, and, in order to measure transient fluxes for each epoch, we first combined the two images in every filter using `uvotimsum`. We then used `uvotsource` to measure counts from the source in the combined images using a 5″0 aperture and a background region of ∼40″0 radius to estimate and subtract the sky background. As with the archival data, we then converted the count rates to magnitudes and fluxes using the most recent UVOT calibration (Poole et al. 2008; Breeveld et al. 2010).

We corrected all of the UVOT photometry for Galactic extinction using a Cardelli et al. (1989) extinction law. To enable the UVOT *B* and *V* data to be directly compared with Johnson *B* and *V* data obtained from ground-based telescopes, we converted the UVOT *B*- and *V*-band data to Johnson *B* and *V* magnitudes using publicly available color corrections.[24] Finally, we then subtracted the host flux measured from the archival *Swift* observations (UV filters and *U*) or taken from the APASS catalog (*BV*) from each UVOT observation to isolate the transient flux in each epoch. The host-subtracted *Swift* UVOT photometry is presented in Table 2 and shown in Figure 3. ASASSN-19bt has one of the brightest measured peak UV magnitudes of any TDE to date, and is comparable in brightness to ASASSN-14li (Holoien et al. 2016b) despite being more distant. ASASSN-19bt also has 10 epochs of UV observations obtained prior to peak, making this one of the

[24] https://heasarc.gsfc.nasa.gov/docs/heasarc/caldb/swift/docs/uvot/uvot_caldb_coltrans_02b.pdf

best-sampled multiwavelength rising light curves obtained to date of a TDE.

2.5. Other Photometric Observations

In addition to the ASAS-SN, *Swift*, and *TESS* observations, we also obtained photometric observations in the *BVri* filters from Las Cumbres Observatory 1 m telescopes located in Cerro Tololo, Chile, Siding Spring, Australia, and Sutherland, South Africa (Brown et al. 2013). After applying photometric calibrations, we measured aperture magnitudes using the IRAF `apphot` package, with a 5.″0 aperture region used to extract source counts and a 15.″0–30.″0 annulus used to estimate and subtract background counts. We calibrated the Las Cumbres Observatory magnitudes using several stars in the field with magnitudes available in the APASS DR 10 catalog.

As we did with the UVOT observations, we corrected the ground-based aperture magnitudes for Galactic extinction and subtracted the host flux in each band taken from APASS. We find excellent agreement between the UVOT *B* and *V* magnitudes and those measured from the Las Cumbres Observatory telescopes. We present the host-subtracted ground-based photometry in Table 2 and show them in Figure 3.

2.6. X-Ray Observations

2.6.1. Swift *XRT Observations*

In addition to the *Swift* UVOT observations, we simultaneously obtained XRT photon-counting (PC) observations of ASASSN-19bt. All observations were reduced following the standard *Swift* XRT data reduction guide,[25] with the level one XRT data reprocessed using the *Swift xrtpipeline* version 0.13.2 script. Standard filters and screening were applied, along with the most up-to-date calibration files. To increase the signal-to-noise of our observations, we also combined the *Swift* observations into five time bins using XSELECT version 12.9.1 c. We used a source region centered on the position of ASASSN-19bt with a radius of 30″, and a source-free background region centered at (α, δ) = (06:59:55.2, −66:05:37.04) with a radius of 150.″0. All extracted count rates were corrected for the encircled energy fraction since this source radius contains only ∼90% of the counts from a source at 1.5 keV (Moretti et al. 2004).

In most epochs, we do not detect X-ray emission from ASASSN-19bt in the XRT data, and we calculate 3σ flux limits from the combined XRT data in such cases. However, in one combined set of observations obtained roughly 2 weeks prior to peak light, we do detect weak X-ray emission from ASASSN-19bt. We report the X-ray luminosity limits and measured luminosities from the combined *Swift* data in Table 3.

2.6.2. XMM-Newton *Observations*

Since the *Swift* XRT observations showed evidence of weak X-ray emission as the source rose to peak, we requested two deep (41.4 ks each) *XMM-Newton Observatory* TOO observations of the source. The first observation was taken on 2019 March 1 (ObsID: 0831791001, PI: Auchettl), approximately 3.5 days before peak ($\mathrm{MJD}_{\mathrm{XMM_1}} = 58{,}543.21$), while the second observation was taken on 2019 April 15 (ObsID: 0831791101, PI: Auchettl), approximately 42 days after peak ($\mathrm{MJD}_{\mathrm{XMM_2}} = 58{,}589$). Both the MOS and PN detectors were used for this analysis, and both detectors were operated in full-frame mode using a thin filter. All data reduction and analysis was done using the *XMM-Newton* science system (SAS) version 15.0.02 with the most up-to-date calibration files.

Due to the fact that *XMM-Newton* suffers from periods of high background and/or proton flares that may affect the quality of the data, we checked for these periods by generating a count rate histogram of the events that have energies between 10 and 12 keV. We find that our observations are only minimally affected by background flares, giving an effective exposure in the PN and MOS detectors of 32 and 37 ks for the first observation and 40 and 39 ks for the second observation.

For our analysis, we used the standard screening of events, with single to quadruple events (PATTERN ⩽ 12) chosen for the MOS detectors. For the PN detector, only single and double events (PATTERN ⩽ 4) were selected. We also used the standard screening FLAGS for both the MOS (#XMMEA EM) and PN (#XMMEA EP) detectors. We corrected for vignetting by processing all event files using the task EVIGWEIGHT. We extracted spectra of ASASSN-19bt from both the MOS and PN detectors using the SAS task EVSELECT and the cleaned event files from all detectors. We used the same source region that was used to analyze the *Swift* observations. To avoid chip gaps, we used a smaller background region centered at (α, δ) = (7:00:38.535, −66:05:43.21) with a radius of 72.″0 for the first observation and (α, δ) = (7:00:06.415, −66:06:31.27) with a radius of 72.″0 for the second observation. To increase the signal-to-noise of the MOS spectra, we combined these spectra together using the SAS task EPICSPECCOMBINE. To analyze the spectra extracted from our *XMM-Newton* observations, we used the X-ray spectral fitting package (XSPEC) version 12.10.1f and χ^2 statistics. Using the FTOOLS command *GRPPHA*, we grouped both the PN and merged MOS spectra with a minimum of 10 counts per energy bin. These data are further discussed in Section 3.4, and the X-ray luminosity measured from the *XMM-Newton* observations is given in Table 3.

Table 3
X-Ray Luminosities (0.3–10.0 keV)

Observation	MJD	Rest-frame Days Relative to Peak	X-Ray Luminosity
Swift 001–005	58521.4	−24.9	$<7.68 \times 10^{40}$
Swift 006–008	58535.7	−10.9	$6.73^{+3.57}_{-3.61} \times 10^{40}$
XMM 0831791001	58543.2	−3.6	$4.48^{+0.77}_{-0.78} \times 10^{40}$
Swift 009–013	58550.0	3.0	$<6.62 \times 10^{40}$
Swift 014–016	58569.6	22.1	$<1.26 \times 10^{41}$
Swift 017–019	58581.4	33.6	$<8.69 \times 10^{40}$
XMM 0831791101	58589.0	−42.1	$1.24^{+0.40}_{-0.38} \times 10^{40}$

Note. X-ray luminosities and 3σ upper limits on the X-ray luminosity from our *Swift* XRT and *XMM-Newton* observations. *Swift* data were binned in time to increase the signal-to-noise of the observations, and the epochs combined for each bin are indicated in Column 1.

2.7. Spectroscopic Observations

After obtaining our first classification spectrum of ASASSN-19bt, we began a program of spectroscopic follow-up to complement our photometric data set. Our follow-up spectra

[25] http://swift.gsfc.nasa.gov/analysis/xrt_swguide_v1_2.pdf

Table 4
Spectroscopic Observations of ASASSN-19bt

Date	Telescope	Instrument	Grating	Slit	Exposure Time
2019 Jan 31.20	Magellan Clay 6.5 m	LDSS-3	VPH-All	1.″00 blue	2 × 600 s
2019 Feb 01.26	du Pont 100 inch	WFCCD	Blue	1.″65	3 × 900 s
2019 Feb 07.03	Magellan Baade 6.5 m	IMACS $f/2$	400 l/mm	1.″20	1 × 300 s
2019 Feb 14.04	Magellan Baade 6.5 m	IMACS $f/2$	300 l/mm	0.″90	2 × 600 s
2019 Feb 15.03	Magellan Baade 6.5 m	IMACS $f/2$	300 l/mm	0.″90	2 × 600 s
2019 Mar 02.02	du Pont 100 inch	WFCCD	Blue	1.″65	3 × 600 s
2019 Mar 04.03	du Pont 100 inch	WFCCD	Blue	1.″65	3 × 600 s
2019 Mar 06.10	du Pont 100 inch	WFCCD	Blue	1.″65	3 × 600 s
2019 Mar 24.05	SOAR 4.1 m	Goodman	400 l/mm	0.″95	1 × 1200 s
2019 Mar 29.00	Magellan Clay 6.5 m	LDSS-3	VPH-All	1.″00 blue	4 × 600 s
2019 Apr 10.20	du Pont 100 inch	WFCCD	Blue	1.″65	3 × 600 s
2019 Apr 13.09	du Pont 100 inch	WFCCD	Blue	1.″65	3 × 600 s

Note. Date, telescope, instrument, grating, slit size, and exposure time for each of the spectroscopic observations obtained of ASASSN-19bt for the initial classification of the transient and as part of our follow-up campaign.

were obtained with LDSS-3 on the 6.5 m *Magellan* Clay telescope, the Inamori-*Magellan* Areal Camera and Spectrograph (IMACS; Dressler et al. 2011) on the 6.5 m *Magellan*-Baade telescope, the Goodman Spectrograph (Clemens et al. 2004) on the Southern Astrophysical Research (SOAR) 4.1 m telescope, and the Wide Field Reimaging CCD Camera (WFCCD) mounted on the du Pont 100 inch telescope. These observations included seven spectra obtained prior to peak light and four spectra obtained within 3 days of peak light.

The majority of our spectra were reduced and calibrated using standard procedures in IRAF, including bias subtraction, flat-fielding, 1D spectroscopic extraction, and wavelength calibration via comparison to an arc lamp. The IMACS data from 2019 February 7 were reduced using an updated version of the routines developed by Kelson et al. (2014) using He and Hg lamps for wavelength calibration. We flux calibrated our observations using standard star spectra obtained on the same nights as the science spectra and masked prominent telluric features. Details of the spectra in our data set are presented in Table 4.

We further calibrated our spectra using our photometric data set. To obtain magnitudes with a similar amount of host contamination as the spectra, which were observed through slits of roughly 1.″0 width, we measured small aperture magnitudes from our *Swift* and Las Cumbres Observatory data, using a 1.″5 aperture for the Las Cumbres Observatory data and a 3.″5 aperture for the *Swift* data, due to the larger pixel scale of *Swift*. For each filter that was completely contained in the wavelength range covered by a given spectrum and for which we could either interpolate the small aperture light curves or extrapolate them by 1 hr or less, we extracted synthetic photometric magnitudes from the spectrum. As the *Swift* data has a larger PSF and the small aperture magnitudes are more uncertain, we calibrated the spectra using only Las Cumbres Observatory data, except for the three spectra taken prior to 2019 February 10, when we obtained our first observations with Las Cumbres Observatory telescopes. We then fit a line to the difference between the synthetic and observed fluxes as a function of central filter wavelength and scaled each spectrum by the photometric fits. Finally, we corrected each spectrum for Galactic reddening using a Milky Way extinction curve assuming $R_V = 3.1$ and $A_V = 0.336$ (Schlafly & Finkbeiner 2011). We also used the procedure to calibrate the archival 6 dF spectrum to the same flux scale as our follow-up spectra using the archival magnitudes shown in Table 1 for calibration.

Figure 5 shows the spectroscopic evolution of ASASSN-19bt as well as the calibrated host spectrum. Prominent telluric bands have been marked in the figure, with the feature from 7550 to 7720 Å and chip gaps (where present) masked to facilitate plotting. Similar to what was seen with PS18kh (Holoien et al. 2018), there is little evidence of broad lines prior to peak light, with the lines becoming more prominent after peak. We further analyze the line emission in Section 3.5.

3. Analysis

3.1. Position, Redshift, and t_{Peak} Measurements

We measured the position of ASASSN-19bt using our initial *V*-band image and a *V*-band image taken near peak from the Las Cumbres Observatory 1 m telescopes. Using the early image as a subtraction template, we generated a subtracted image of the TDE. While some TDE flux was likely removed along with the host flux, this allowed us to measure a centroid position of only the TDE signal. Using the IRAF task `imcentroid`, we measured the centroid position of the flux in the subtracted image as well as the centroid position of the nucleus of the host galaxy in the early *V*-band image that was used as the subtraction template, which is likely host-dominated. From this method, we obtain a position for ASASSN-19bt of R.A. = 07:00:11.41, decl. = −66:02:25.16. This is offset by 0.″14 ± 0.″15 from the position of the host nucleus measured from the early image, which corresponds to a physical offset of 78.2 ± 83.8 pc.

The redshift of the host galaxy in the 6 dF catalog is reported as $z = 0.0262$. In order to verify this, we downloaded the 6 dF spectrum and measured the redshift using the narrow Hα and [O III] 5007/4959 Å emission lines, finding $z = 0.026$. As this is consistent with the reported redshift, we adopt $z = 0.0262$ and the corresponding luminosity distance of $d = 115.2$ Mpc throughout our analysis.

To obtain an estimate of the time of peak light, we fit a parabola to the host-subtracted ASAS-SN *g*-band light curve prior to MJD = 58,560, as the decline of the light curve is flatter than the rise, making a parabolic fit to the entire light curve inaccurate. To estimate the uncertainty on the peak date, we generated 10,000 realizations of the *g* light curve prior

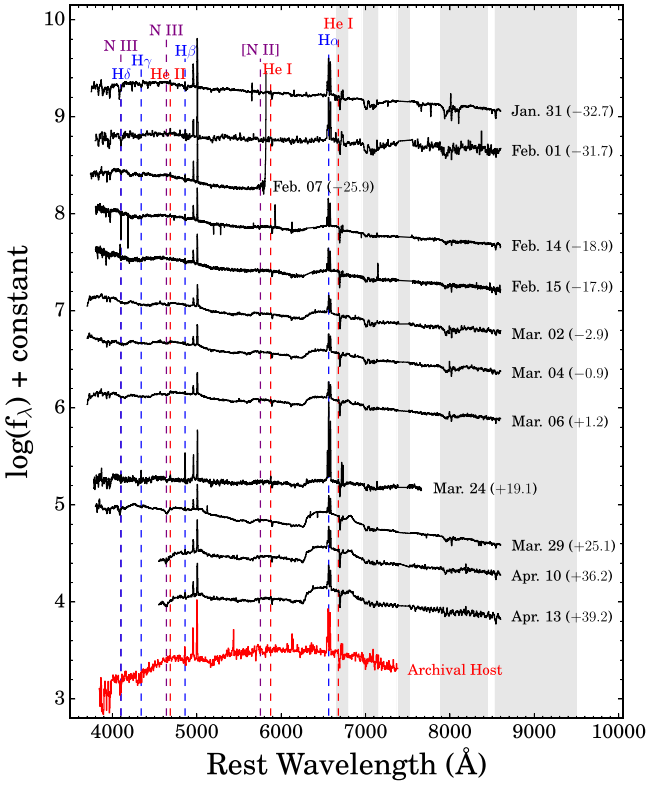

Figure 5. Spectroscopic evolution of ASASSN-19bt spanning from 33 days prior to peak (2019 March 04) through 36 days after peak. All spectra have been flux calibrated using our photometry, as described in Section 2.7. The date for each spectrum and phase relative to peak in observed days is shown next to each spectrum. Hydrogen, helium, and nitrogen features that are common to TDEs are indicated with blue, red, and purple dashed lines, respectively. Telluric bands are shown in light gray. The calibrated archival host spectrum from 6 dF is shown in red.

(The data used to create this figure are available.)

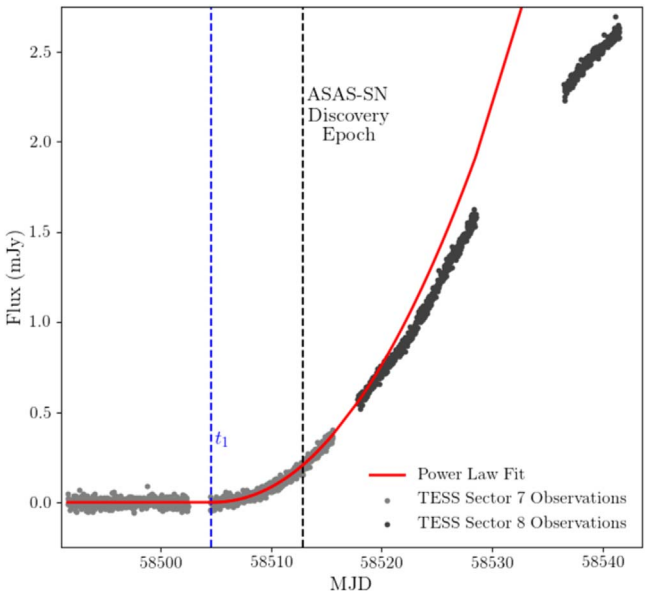

Figure 6. The *TESS* image subtraction light curve of ASASSN-19bt obtained during Sector 7 and Sector 8. Individual flux measurements obtained for each FFI are shown in gray, with different shades denoting each sector, and a best-fit power-law model to the Sector 7 data is shown in red. This power-law fit yields a time of first light of $t_1 = 58504.61 \pm 0.42$ and has an index of $\alpha = 2.10 \pm 0.12$. The blue dashed line and black dashed line show the inferred t_1 and the ASAS-SN discovery date, respectively. The light curve begins to diverge from the initial power-law evolution roughly 15 days after first light.

to MJD = 58,560 with each magnitude perturbed by its uncertainty assuming Gaussian errors. We then fit a parabola to each of these light curves and calculated the 68% confidence interval and median $t_{\rm peak}$ values from these realizations. Using this procedure, we find $t_{g,\rm peak} = 58546.9 \pm 0.2$ and $m_{g,\rm peak} = 14.9$. We also performed the same analysis for all of our photometric filters and found that there is some evidence that the bluer filters peaked earlier, with $t_{UVW2,\rm peak} = 58544.2^{+2.6}_{-1.9}$ and $t_{i,\rm peak} = 58548.9^{+2.4}_{-1.5}$, not unlike what has been seen in some other TDEs (e.g., Holoien et al. 2018). Due to the high cadence of the ASAS-SN light curve, its peak is much better constrained than those of the other filters, and we adopt the *g*-band peak of $t_{g,\rm peak} = 58546.9$, corresponding to 2019 March 04.9, throughout this paper.

3.2. Light-curve Analysis

We characterized the early-time rise of ASASSN-19bt with a power-law model

$$f = z \text{ when } t < t_1, \text{ and} \quad (1)$$

$$f = z + h\left(\frac{t - t_1}{\rm days}\right)^{\alpha} \text{ when } t > t_1. \quad (2)$$

for the *TESS* flux, described by a residual background z, the start of the rise t_1, a flux scale h, and the power-law index α. We use the SCIPY.OPTIMIZE.CURVE_FIT package's Trust Region Reflective method to obtain a best-fit model with parameters $z = -0.22 \pm 0.22\,\mu$Jy, $h = 2.44 \pm 0.90\,\mu$Jy, $t_1 = \text{MJD} = 58504.61 \pm 0.42$, and $\alpha = 2.10 \pm 0.12$. This fit is shown as the red curve in Figure 6.

This power-law index is consistent with the "fireball" model used to model the early flux from SNe where

$$L_\nu \propto r^2 T \propto v^2 (t - t_1)^2 T, \quad (3)$$

which assumes a band on the Rayleigh–Jeans tail of the SED and homologous expansion. For the early phases of SNe, this power-law rise with $L_\nu \propto (t - t_1)^2$ is due to the fact that the velocity v and temperature T are nearly constant (e.g., Riess et al. 1999; Nugent et al. 2011). However, as we shall see in Section 3.3, the temperature of ASASSN-19bt does not appear to be constant in these early phases, so the consistency of the exponent α with the fireball model appears coincidental.

Given the distance to the source and the effective wavelength of the *TESS* bandpass, the flux scale given by the fit implies a radius of

$$r = 10^{13.9} T_4^{-1/2} (t - t_1)^{1.05} \text{ cm} \quad (4)$$

for a temperature of $T = 10^4 T_4$ K, the central values of h and α and assuming Equation (3). For our estimated black hole mass, this corresponds to $100 T_4^{-1/2}$ gravitational radii at $t - t_1 =$ 1 day. Since the emission region is probably not spherical, it is probably more accurate to say that the surface area producing the UV/optical emission is $4\pi r^2$.

The *TESS* light curve begins to deviate from the initial power-law rise approximately 15 days after first light, with the rise slowing as it approaches peak brightness. Based on the

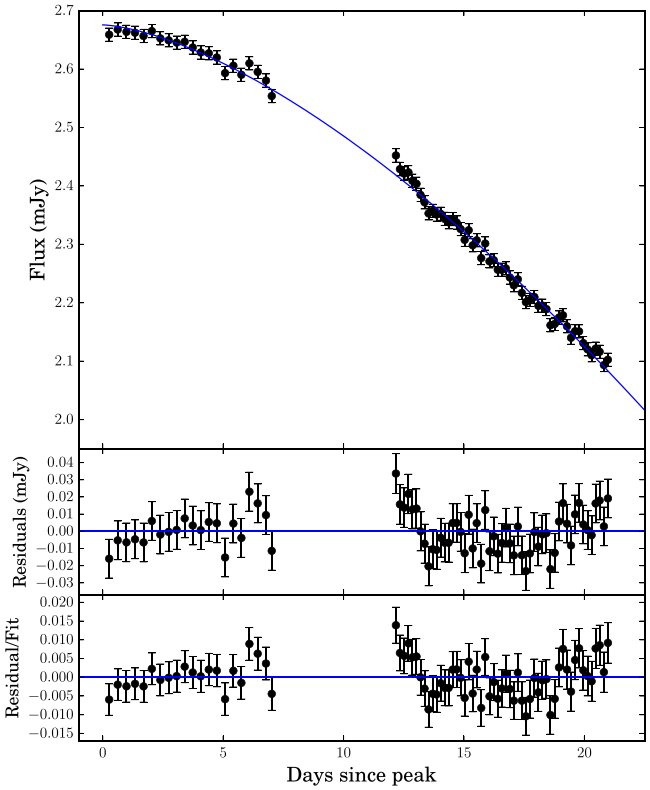

Figure 7. The post-peak *TESS* light curve and best-fit power-law model (top panel). The middle and lower panels show the fit residuals and residuals/flux, respectively.

inferred time of first light taken from the power-law fit and the time of peak light measured from the ASAS-SN light curve, we constrain the rise time to 41.2 ± 0.5 rest-frame days.

The photometric precision of the *TESS* light curve, particularly with the addition of the Sector 9 data, allows us to see clearly that the TDE light curve is very smooth, with little to no short-term variability. This is in contrast to what is often seen during AGN flares (e.g., Peterson 1993; Peterson et al. 2004; Shappee et al. 2014). While the light curves from ASAS-SN and Las Cumbres Observatory are also quite smooth, the *TESS* cadence provides us with a unique ability to see exactly how smooth the light curve is. To take advantage of this, we fit the *TESS* Sector 9 light curve taken after peak light with a power-law decline of the form

$$f = z - h\left(\frac{t - t_{\rm peak}}{\rm days}\right)^{\alpha} \quad (5)$$

with $t_{\rm peak}$ being the peak date inferred from the ASAS-SN light curve.

The best-fit power law has the parameters $z = 2.68\,\mu$Jy, $h = 0.006\,\mu$Jy, and $\alpha = 1.53$, with a reduced chi-squared value of $\chi^2_\nu = 1.05$. The *TESS* declining light curve and best-fit model are shown in Figure 7. The fit residuals are roughly 1% or less of the actual flux, with an rms value of 0.01, implying that deviations from the power-law fit are likely systematic. The fact that the light curve is very well fit by a simple model such as this demonstrates the smoothness of the light curve in a way that was not previously possible.

3.3. SED Evolution

To better understand the physical parameters of the transient, we modeled the UV and optical SED of ASASSN-19bt for epochs where *Swift* data were available as a blackbody. We used Markov Chain Monte Carlo methods to fit the blackbody SED, using a flat prior of $10{,}000\,{\rm K} \leqslant T \leqslant 55{,}000\,{\rm K}$ so as not to overly influence the fits. From the blackbody fits, we estimate the bolometric luminosity, temperature, and radius of ASASSN-19bt in each epoch.

To take better advantage of the high-cadence light curve from ASAS-SN, we used the *Swift* blackbody fits to calculate bolometric corrections for *g*-band magnitudes by linearly interpolating between the previous and next *g*-band measurements bracketing each epoch of *Swift* observations. We then estimated the bolometric luminosity of ASASSN-19bt from the ASAS-SN light curve, by linearly interpolating bolometric corrections calculated for the *Swift* epochs to each epoch of *g* data. For times prior to our first *Swift* observation, we use the bolometric correction from the first *Swift* sED fit. The luminosity evolution calculated from the *Swift* sED fits and estimated from the *g*-band light curve is shown in the left panel of Figure 8.

The luminosity fits and corrected *g*-band light curve indicate that both the rise to peak and then initial decline after peak are relatively smooth. However, the first *Swift* sED fit indicates that the luminosity was higher in the first epoch than it was in the second, resulting in a short decline at $t \simeq -32$ rest-frame days before peak. This corresponds to a similar drop in the early temperature (see below). Such behavior has not been seen in TDEs prior to ASASSN-19bt. However, *Swift* UV data has not been obtained at such early times prior to peak for previous TDEs. This makes it unclear whether an early, rapid drop in temperature and luminosity is common in TDEs, or unique to ASASSN-19bt, and further highlights the need for early detection and prompt scheduling of follow-up observations.

The early luminosity spike is not seen in the uncorrected *g*-band data, and the rapid rise to this early peak shown in Figure 8 is driven by the fact that we used the first *Swift* luminosity fit to calculate the bolometric correction for all of the previously obtained epochs of *g*-band data. Due to the 10 day gap between our second and third *Swift* observations, it is also difficult to determine precisely when the luminosity begins to rise again. However, we can say that the early luminosity spike must have lasted for at least 2 days and could have been as long as roughly 15 days, depending on how rapid the rise actually was and when it stopped declining and began to re-brighten. We also note that while the luminosity began to re-brighten sometime between -30 and -20 days prior to peak, its temperature continued to drop during this time, resulting in an early temperature decline that lasted at least 12 rest-frame days.

In the right panel of Figure 8, we show a comparison of the light-curve evolution of ASASSN-19bt to that of several other TDEs from the literature: ASASSN-14ae (Holoien et al. 2014), ASASSN-14li (Holoien et al. 2016b), ASASSN-15oi (Holoien et al. 2016a), iPTF16fnl (Brown et al. 2018), iPTF16axa (Hung et al. 2017), PS18kh (Holoien et al. 2018), and ASASSN-18pg (T. W.-S. Holoien et al. 2019, in preparation; Leloudas et al. 2019). The luminosity rise of ASASSN-19bt is similar to those of ASASSN-18pg and PS18kh with the exception of the spike at $t = -32$ days, and it begins to decline more rapidly after peak than ASASSN-18pg, which has a plateau-like phase at

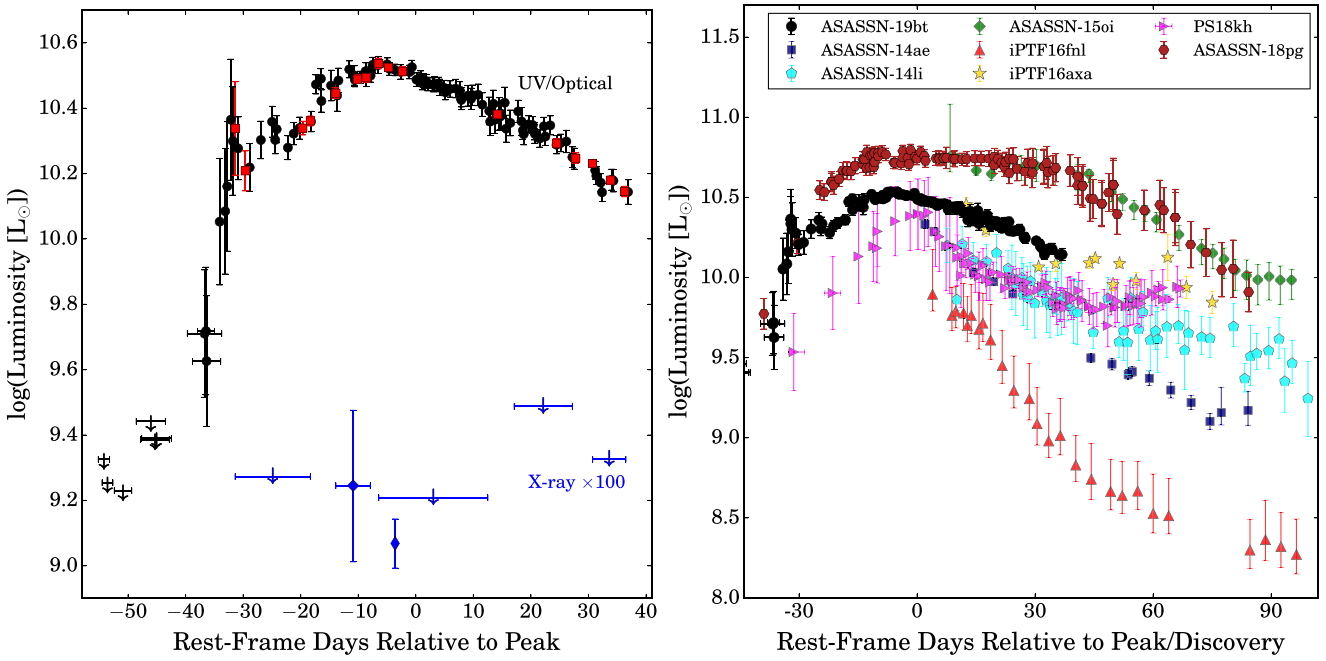

Figure 8. Left panel: evolution of the luminosity of ASASSN-19bt from blackbody fits to the UV/optical *Swift* sED (red squares) and estimated from the ASAS-SN *g*-band data by applying bolometric corrections based on the *Swift* fits (black circles). *Swift* XRT and *XMM-Newton* X-ray luminosities are shown as wide and thin blue diamonds, respectively, multiplied by a factor of 100 to improve readability. *X*-axis error bars indicate data ranges for data combined to obtain a single measurement, and downward arrows indicate upper limits. Right panel: comparison of the luminosity evolution of ASASSN-19bt (black circles) to that of the TDEs ASASSN-14ae (navy squares; Holoien et al. 2014), ASASSN-14li (cyan penatgons; Holoien et al. 2016b), ASASSN-15oi (green diamonds; Holoien et al. 2016a), iPTF16fnl (red triangles; Brown et al. 2018), iPTF16axa (gold stars; Hung et al. 2017), PS18kh (magenta right-facing triangles; Holoien et al. 2018), and ASASSN-18pg (brown hexagons; T. W.-S. Holoien et al. 2019, in preparation). Time is shown in rest-frame days relative to peak for those objects that have observations spanning the peak of the light curve (ASASSN-19bt, ASASSN-18pg, and PS18kh) and in days relative to discovery for those objects that do not (ASASSN-14ae, ASASSN-14li, ASASSN-15oi, and iPTF16fnl).

peak. Both the decline rate shortly after peak and the total luminosity are similar to most of the other objects in the sample, and ASASSN-19bt peaked at a luminosity of $L \simeq 1.3 \times 10^{44}\,\mathrm{erg\,s^{-1}}$.

Figure 8 also shows the X-ray luminosities calculated from the *Swift* XRT and *XMM-Newton* observations, scaled up by a factor of 100 to make them comparable to the UV/Optical luminosities. We do not detect X-ray emission in most epochs, and all detected luminosities are three or more orders of magnitude weaker than the UV/optical emission. We also see some evidence that X-rays are only detected near the peak of the UV/optical light curve. We further analyze and discuss the X-ray results in Section 3.4 below.

We show the SEDs and blackbody fits for the first three *Swift* epochs in Figure 9. The SED for the median luminosity and the range corresponding to the 16%–84% confidence interval on the luminosity are also shown. The emission clearly becomes redder over these 12 days, with the *UVW2* flux becoming fainter relative to the *UVM2* flux over time. After −20 days, the TDE continues to exhibit the highest luminosity in the *UVM2* filter, which drives the cooler temperature fits up to and shortly after peak.

Integrating the entire rest-frame bolometric light curve, including both the *Swift* blackbody fits and the converted *g*-band data, we obtain a total radiated energy of $E = (5.92 \pm 0.06) \times 10^{50}$ erg. Of this, $(3.17 \pm 0.05) \times 10^{50}$ erg are released during the rise to peak, indicating that a large fraction of the energy radiated by TDEs can be emitted prior to peak light. The accreted mass required to generate the emitted energy is $M_{\rm Acc} \simeq 0.003\eta_{0.1}^{-1} M_{\odot}$, where the accretion efficiency is $\eta = 0.1\eta_{0.1}$. This low implied accreted mass is similar to what

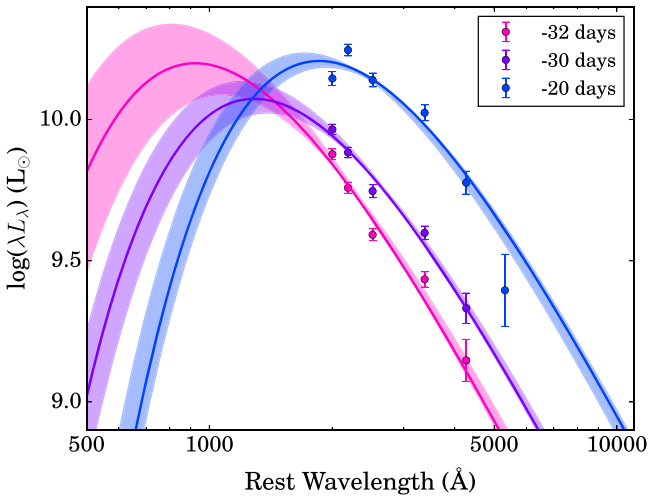

Figure 9. The first three *Swift* epochs and their blackbody fits. The solid lines show the SEDs of the median luminosity fits to each epoch, and the shaded regions show the range of SEDs for the 16%–84% confidence interval on the luminosity. The phase in rest-frame days relative to peak is given in the legend.

has been seen in other TDEs and again indicates that either only a small fraction of the bound stellar material is actually accreting onto the SMBH, or that the material accretes with very low radiative efficiency.

The blackbody temperature evolution of ASASSN-19bt is shown in Figure 10, along with that of the same TDE comparison sample shown in Figure 8. Unique among the TDEs shown in the figure, ASASSN-19bt exhibits a steep temperature decline in the first three epochs, corresponding to

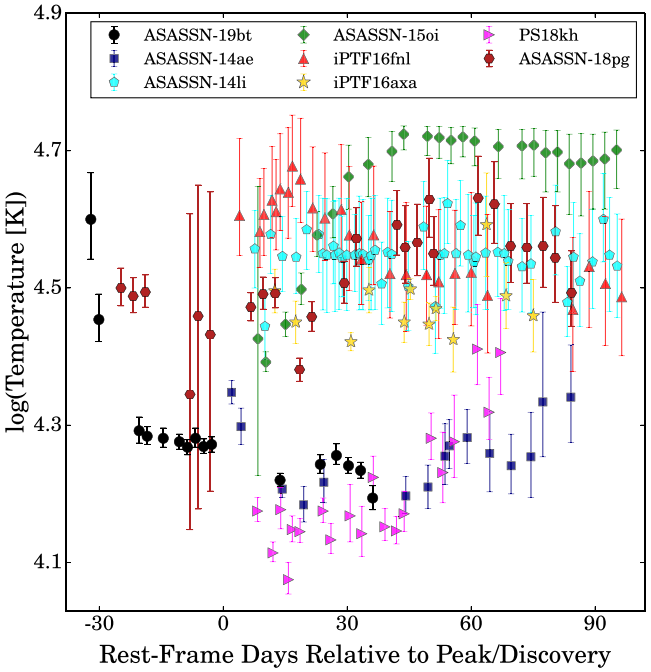

Figure 10. Temperature evolution of ASASSN-19bt from the *Swift* blackbody fits (black circles) compared with that of the objects in our TDE comparison sample. Time is in days relative to peak light or relative to discovery, as outlined in the caption of Figure 8, and the symbols and colors match those of Figure 8.

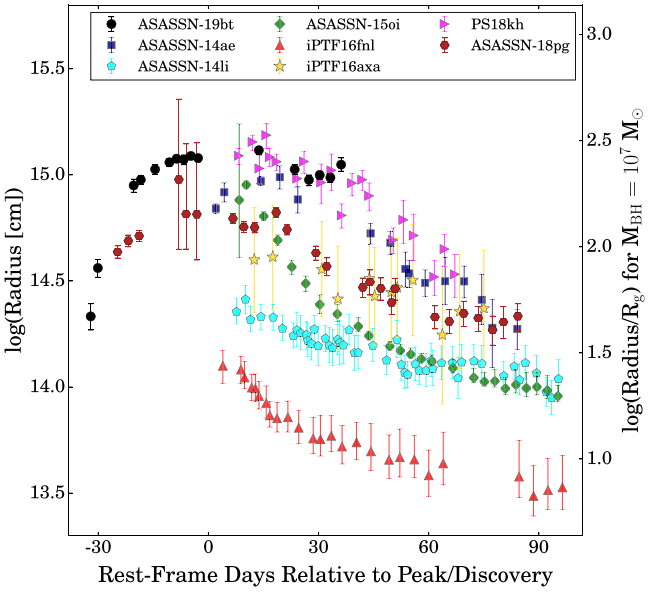

Figure 11. Blackbody radius evolution of ASASSN-19bt from the *Swift* fits (black circles) compared with the radius evolution of the objects in our TDE comparison sample. Time is in days relative to peak light or relative to discovery, as outlined in the caption of Figure 8, and the symbols and colors match those of Figure 8. The left-hand scale shows the radius in units of cm, while the right-hand scale shows the same scale in units of the gravitational radius for a $10^7\ M_\odot$ black hole.

the luminosity decline over the same period before leveling off and exhibiting the relatively constant temperature evolution that is expected. None of the comparison objects have UV data as early as ASASSN-19bt, so it is possible that an early drop in temperature is common but not observed due to discovering the TDE flare too late. After the initial decline, the temperature remains fairly steady at $T \simeq 16{,}000$–$17{,}000$ K, on the low end of the temperature range observed for TDEs.

Figure 11 shows the blackbody radius evolution of ASASSN-19bt taken from the *Swift* fits compared to the radius evolution of the other TDEs in our comparison sample. ASASSN-19bt exhibits a rapidly growing radius in the first three epochs to match the drop in temperature over the same timeframe. It then appears to peak and hold relatively steady for the remainder of our period of observation at one of the largest radii of the TDEs in our sample. While there does not seem to be a strong correlation between size and rate of decline in radius, it appears that the hotter TDEs tend to have smaller emitting regions, which is not unexpected given that they are have similar luminosities. ASASSN-19bt is a very close match to PS18kh in both temperature and radius evolution, and it will be interesting to see if ASASSN-19bt exhibits a similar "re-brightening/plateau" phase later in its evolution.

We can also combine the radius estimates from the SED fits with the results from fitting the *TESS* light curve in Section 3.2, as shown in Figure 12. Here, we work in terms $t-t_1$ based on the onset time found in the *TESS* fits. The *TESS* radius estimate depends on the temperature, and we show two simple assumptions. We either assume the temperature found for the first *Swift* epoch ($\log(T/\mathrm{K}) = 4.60$) or the power law in temperature defined by the first two *Swift* epochs ($\log(T/\mathrm{K}) = 6.66$–$2.06\log(t-t_1)$) in order to illustrate the uncertainties. Where they overlap, the two sets of radius estimates agree reasonably well (factor of ∼2). At the time of our earliest *TESS*

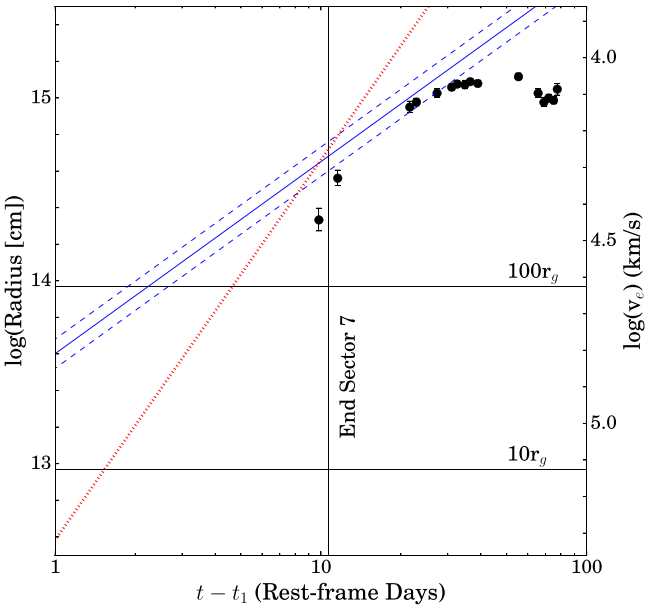

Figure 12. Radius evolution in rest-frame days from the estimated start of the *TESS* emission. The points show the results from the SED fits. The solid blue line bracketed by blue dashed lines shows the radius estimate from the *TESS* light curve assuming the temperature of the first *Swift* epoch, while the dotted red line shows the radius estimate assuming a power-law decline in temperature based on the first two *Swift* epochs. The dashed lines illustrate the scale of the uncertainties from the h parameter of the *TESS* light curve fits. The scale on the right is the escape velocity assuming a BH mass of $10^{6.8} M_\odot$. A vertical line marks the end of *TESS* Sector 7, and horizontal lines show the radii corresponding to 10 and 100 gravitational radii given our BH mass estimate.

detection, when $t-t_1 \sim 2$ days, the emission region probably had an effective size of some tens of gravitational radii.

Figure 12 also shows the escape velocity corresponding to a given radius assuming a BH mass of $10^{6.8} M_\odot$. For the constant-temperature case, the *TESS* radius evolution corresponds to a

velocity of $\sim$2700 km s^{-1}, which is well below the scale of the escape velocity and well above the sound speed implied by the temperatures. With the rapidly evolving temperature, the velocity implied by the *TESS* radius is 870 $(t-t_1)^{1.08}$ km s^{-1}, so accelerating from 870 km s^{-1} on day 1 to 10,500 km s^{-1} on day 10. Similarly, the $\sim 10^{14.5}$ cm sizes implied by the first few *Swift* epochs also only require velocities of 3000–4000 km s^{-1}. Thus, if the early-time radii implied either by the *TESS* flux evolution or the first few SED fits are related to the distance from the black hole, the apparent photosphere is expanding very slowly compared to the local escape speed. If these velocities are related to dynamical velocities, then the emission region must be at a distance near $10^{16.3}$ cm from the BH and the emission region is very small compared to the distance.

3.4. X-Ray Analysis

During the first $\sim$two weeks of its evolution, our *Swift* XRT observations of ASASSN-19bt showed no evidence of X-ray emission. We first detect the source approximately two weeks prior to the peak, the first such detection. For those events that do show evidence of X-ray emission (e.g., ASASSN-14li, Holoien et al. 2016b; Brown et al. 2017; ASASSN-15oi, Holoien et al. 2016a, 2018; Gezari et al. 2017; ASASSN-18ul, Wevers et al. 2019; and those in Auchettl et al. 2017), the X-ray emission is first detected at or after peak. However, some of these events may have had emission at or before peak, as most X-ray observations of these sources only commenced as the associated optical/UV transient began to decline. For the other two events that were detected on the rise in the optical/UV, *Swift* XRT observations were taken after peak and showed that PS18kh (Holoien et al. 2019b; van Velzen et al. 2019) exhibited weak X-ray emission. Pre-peak *Swift* observations of ASASSN-18pg only yielded upper limits on the presence of X-ray emission (Leloudas et al. 2019, T. W.-S. Holoien et al. 2019, in preparation).

There are too few counts in the XRT detections to extract a spectrum, but we could determine the hardness ratio, HR = (H− s)/(H+S), where S is the number of counts in the soft 0.3–2.0 keV energy band and H is the number of counts in the 2.0–10.0 keV energy band. A source is considered soft if it has an HR = −1, while it is considered hard if it has an HR = 1. Interestingly, we find an average hardness ratio of HR $\sim$ −0.2, which is much harder than found for non-jetted, thermal TDEs like ASASSN-14li and ASASSN-15oi, which have HR $\sim$ −0.7, and more consistent with those seen from the jetted TDEs Swift J1644+57 and Swift J2058-05 (Auchettl et al. 2017; Holoien et al. 2018).

Due to the hardness of this X-ray emission, we triggered two deep *XMM-Newton* TOO observations of the source to better constrain its nature. The first observation was taken $\sim$4 days before peak, while the second observation was take $\sim$42 days after peak, and in both observations, the source is significantly detected. The shallower *Swift* observations taken around this time were only able to determine upper limits due to the faintness of this emission. In Figure 13, we show the resulting PN and MOS1+MOS2 spectra. In the first observation (Figure 13 top panel), the spectra are well fit by an absorbed power-law model with a photon index of $\Gamma = 1.47 \pm 0.3$ and the Galactic H I column density in the direction of ASASSN-19bt (Kalberla et al. 2005). Letting the column density ($N_{\rm H}$) vary does not significantly improve the fit. This photon index is consistent with the best-fit photon index for the jetted TDE

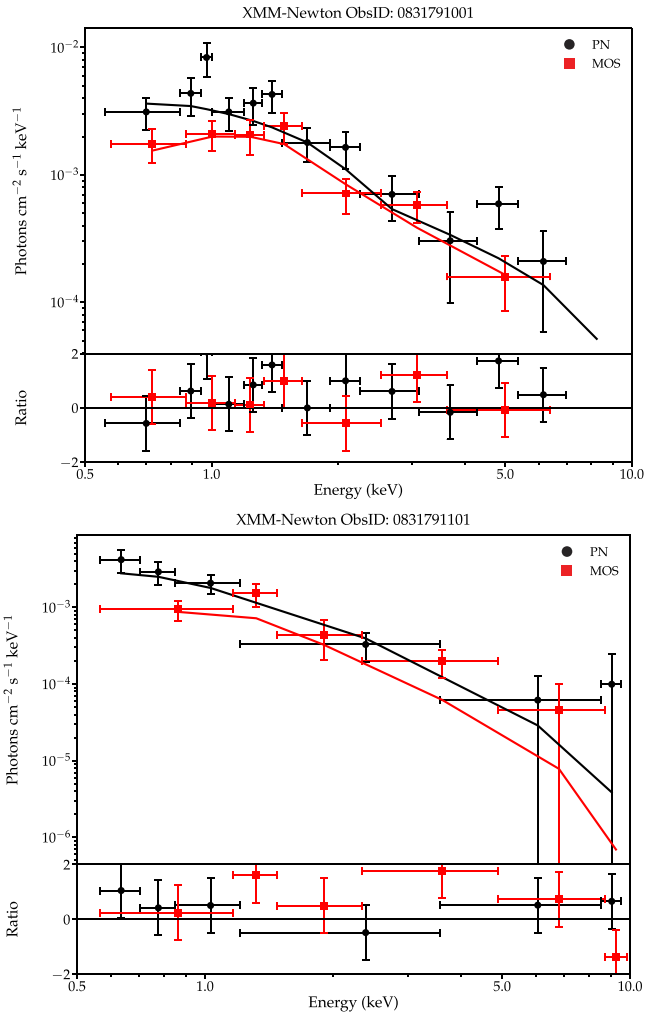

Figure 13. *XMM-Newton* PN (black) and merged MOS1+MOS2 (red) spectra of ASASSN-19bt taken $\sim$4 days before peak (top panel) and $\sim$42 days after peak (bottom panel). Each spectrum is binned to have 10 counts per energy bin. (a) The emission from ASASSN-19bt before peak is well fit by an absorbed power law with a photon index of $\Gamma = 1.48 \pm 0.3$, while after peak, the emission is well fit with an absorbed power law with a photon index of $\Gamma = 2.34^{+0.8}_{-0.6}$. The residuals from the fit are shown in the bottom panel of each figure.

Swift J1644+57 and Swift J2058+05 at late times (e.g., Burrows et al. 2011; Cenko et al. 2012b; Saxton et al. 2012; Levan et al. 2016; Auchettl et al. 2017) and those found from AGN (e.g., Ricci et al. 2017; Auchettl et al. 2018), implying that the X-ray emission may indicate the presence of a jet. The X-ray emission of several TDEs is well-modeled by a cool blackbody. A blackbody fit to the spectrum of ASASSN-19bt gives a temperature of 0.48 ± 0.1 keV. This is significantly higher than the temperatures found for ASASSN-14li (e.g., Brown et al. 2016; Kara et al. 2018) or ASASSN-15oi (Holoien et al. 2018), which have temperatures of $\sim$50 eV. Due to the poor signal-to-noise of the spectra, models combining a blackbody with a power law do not improve significantly on our best-fit power-law model. In the second observation (Figure 13 bottom panel), we find that the X-ray emission has softened considerably after peak and is now well fit by an absorbed power-law model with a photon index of $\Gamma = 2.34^{+0.8}_{-0.6}$ but still consistent with those found from jetted TDES (e.g., Burrows et al. 2011; Cenko et al. 2012b; Saxton et al. 2012; Auchettl et al. 2017). If we fit the spectra using a

Table 5
Measured Line Luminosities

Rest-frame Days Relative to Peak	Hα Luminosity	He I Luminosity	Broad Blue Feature Luminosity
−18.39	$(2.00 \pm 0.60) \times 10^{41}$	$(0.55 \pm 0.17) \times 10^{41}$	$(2.21 \pm 0.66) \times 10^{41}$
−17.42	$(1.91 \pm 0.57) \times 10^{41}$	$(0.61 \pm 0.18) \times 10^{41}$	$(2.33 \pm 0.70) \times 10^{41}$
−2.81	$(3.31 \pm 0.99) \times 10^{41}$	$(0.85 \pm 0.25) \times 10^{41}$	$(2.64 \pm 0.79) \times 10^{41}$
−0.86	$(3.64 \pm 1.09) \times 10^{41}$	$(0.89 \pm 0.27) \times 10^{41}$	$(4.25 \pm 1.27) \times 10^{41}$
1.16	$(3.86 \pm 1.16) \times 10^{41}$	$(1.00 \pm 0.30) \times 10^{41}$	$(3.00 \pm 0.90) \times 10^{41}$
18.65	$(2.48 \pm 0.74) \times 10^{41}$	$(0.55 \pm 0.17) \times 10^{41}$	...
24.44	$(6.01 \pm 1.80) \times 10^{41}$	$(0.76 \pm 0.23) \times 10^{41}$	$(5.69 \pm 1.71) \times 10^{41}$
35.26	$(5.00 \pm 1.50) \times 10^{41}$	$(0.7 \pm 0.21) \times 10^{41}$	$(6.87 \pm 2.06) \times 10^{41}$

Note. Line luminosities of the Hα and He I 5875 Å lines and the broad blue feature spanning Hβ, He II 4686 Å, and Hγ measured from the follow-up spectra of ASASSN-19bt. All luminosities are quoted in erg s^{-1}. The broad blue feature was not measurable in all epochs, and no lines were measurable in the spectra taken prior to 2019 February 12. The uncertainties are 30% uncertainties on the measured fluxes.

blackbody instead, we find a slightly lower temperature of 0.20 ± 0.1 keV compared to the first observation, but it is still higher than that found for other TDEs. Similar to the first observation, fitting the spectra with a blackbody plus a power law does not significantly improve the fit.

3.5. Spectroscopic Analysis

ASASSN-19bt exhibits several broad emission lines that begin to emerge following the 2019 February 07 spectrum, prior to which there are no discernible features. We identify strong emission from Hα, He I 5875 Å, and a broad blue feature that spans the Hβ, He II 4686 Å, and Hγ lines. In later epochs, the broad blue feature can be differentiated into likely Hβ and Hγ lines, and it is apparent that there is little to no emission from the He II 4686 Å line, which is a rarity among TDEs. There is no sign of emission from any of the nitrogen lines identified by Leloudas et al. (2019) in any epoch, meaning ASASSN-19bt is not among the subset of nitrogen-rich TDEs. The Hα and He I 5875 Å lines are extremely broad once they begin to emerge, with maximum FWHM of $\mathrm{FWHM_{H\alpha}} \simeq 2.7 \times 10^4\,\mathrm{km\,s^{-1}}$ and $\mathrm{FWHM_{He\,I}} \simeq 2.1 \times 10^4\,\mathrm{km\,s^{-1}}$. The lines continue to exhibit similar widths throughout the period of observation and begin to develop significantly non-Gaussian shapes in later epochs.

We also measured the luminosities of the prominent emission lines in the epochs after the 2019 February 7 spectrum. For each spectrum, we subtracted a local continuum estimate for the Hα and He I 5875 Å lines, then measured the integrated line flux using the IRAF task `splot`. We also used the same procedure to measure the broad blue feature as a single emission line when possible, as this feature is difficult to break down into its component lines, making it difficult to measure the lines individually. The measured luminosities are given in Table 5 and are shown in Figure 14. Estimating the true error on the line fluxes is difficult given their complex shape, and we assume 30% errors on the emission fluxes calculated from each epoch.

The broad lines appear roughly 18 days prior to peak and continue to grow stronger throughout the period of observation, with the Hα luminosity roughly tripling between the first detections and the latest spectrum from 2019 April 10. The emergence of spectroscopic emission lines prior to peak light and the continuing strengthening of those lines after peak is similar to what was seen with the TDE ASASSN-18pg (Leloudas et al. 2019), although in that case the lines were present more than 30 days prior to peak. Increasing line

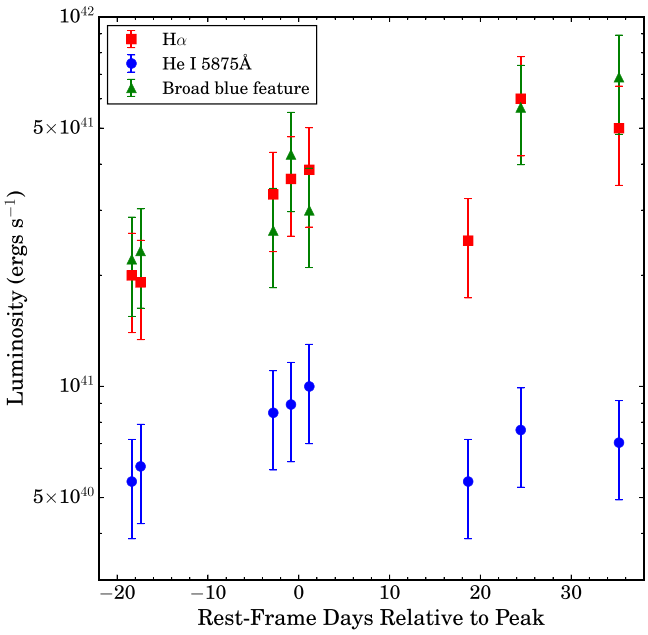

Figure 14. Evolution of the Hα (red squares) and He II 5875 Å (blue circles) line luminosities and the luminosity of the broad blue emission feature (green triangles) in the spectra of ASASSN-19bt. Error bars show 30% errors on the line fluxes. Only epochs where the lines are measurable are shown.

luminosities after peak were also seen in the TDE PS18kh; though in that case, the lines were not present until roughly peak light (Holoien et al. 2018). ASASSN-19bt thus joins a growing sample of TDEs with early spectra that exhibit increasing line luminosities near peak light, in contrast to early TDE discoveries that were found after peak and showed lines that became less luminous in the epochs following discovery (e.g., Holoien et al. 2016b; Brown et al. 2017).

The cause for the early, featureless spectra we observe in ASASSN-19bt is not well understood at this time, in part due to the small number of TDEs with spectra obtained this early. But one possible explanation is that at very early times, the material emitting the lines may be moving at very high speeds, as indicated in Figure 12, which would have the effect of suppressing these features. Further analysis on a larger sample of pre-peak TDE spectra is needed to determine whether other physical effects could play a role in suppressing early line emission, particularly if different TDEs are producing emission

via different physical mechanisms, as some of the observations seem to indicate.

4. Discussion

ASASSN-19bt is the first TDE detected by *TESS*, and, as it happened to fall in the CVZ, it presents us with an unprecedented rising light curve for a TDE. Furthermore, due to its early detection by ASAS-SN only a few days after beginning to brighten, we were able to collect a wide variety of observations prior to peak, including several optical spectra and 10 epochs of *Swift* UVOT and XRT observations. All of these observations combine to make ASASSN-19bt by far the best-observed TDE at early times, and they allow us to look at its early evolution in new ways.

While ASASSN-19bt exhibits luminosity, temperature, radius, and spectroscopic evolution all similar to those of other TDEs, it stands out in several ways. Its host appears to be similar to the population of "shocked post-starburst" galaxies, a sample of galaxies that are likely to have had a recent episode of star formation, similar to the E+A hosts seen for several other TDEs, but which are typically younger and have higher dust obscuration. Our earliest *Swift* observations, obtained more than a month prior to peak, indicate that at very early times, the TDE cooled and faded, before the temperature leveled off and the luminosity began to rise again to peak. Based on our data, we can constrain the duration of the early luminosity bump to be 2–15 rest-frame-days and the duration of the early temperature decline to be at least 12 rest-frame days. This behavior has not been seen in any other TDE, but this may be due to the fact that no TDE has had *Swift* observations at such early epochs.

ASASSN-19bt has weak X-ray emission, and our deep observations with *XMM-Newton* indicate that its X-ray emission is hard compared to that of other thermal TDEs. This may indicate the presence of a jet, as the best-fit photon index is very similar to those found for the jetted TDEs Swift J1644+57 and Swift 2058+05 (e.g., Burrows et al. 2011; Cenko et al. 2012b; Saxton et al. 2012; Auchettl et al. 2017). The fact that the emission softens after peak may indicate that prior to peak, we are are seeing the stellar debris being expelled in a fast collimated outflow reminiscent of a jet, which then circularises and forms an accretion disk around peak. After peak, the softer photon index may indicate that the hard X-ray emission from the jet is reprocessed by the disk into longer X-ray wavelengths, leading to the shallower photon index, or that the X-ray emission after peak is now dominated by the disk in the form of a soft blackbody component. Due to the poor signal-to-noise of our second *XMM-Newton* observation, we cannot distinguish the jet (power law) and disk (blackbody) components sufficiently. The softening of the X-ray emission seen from ASASSN-19bt after peak is reminiscent of hard and soft states seen in X-ray binaries, where the soft state is dominated by blackbody emission from the disk and the hard state is dominated by a power law arising from a jet (e.g., see the review by Remillard & McClintock 2006).

Similar to what was seen with the TDE PS18kh (Holoien et al. 2019b), ASASSN-19bt shows no spectroscopic emission features in its earliest spectra. The broad lines only develop as the TDE approaches peak light. Once they appear, we see broad, asymmetric Balmer lines and clearly detect the He I 5875 Å line. Although it is a common feature of TDE spectra, there is no discernible He II 4686 Å line.

The *TESS* light curve allows us to place a strong constraint on when the TDE began to brighten, and we find that the time between first light and the peak of its light curve was 41 rest-frame days. The very early rise in the *TESS* flux is well fit by a power law that is consistent with the t^2 "fireball" model found for the early rise of supernovae. However, since the temperature of ASASSN-19bt does not appear to be constant during this time, the consistency with the fireball model is likely coincidental. The *TESS* light curve and early *Swift* sED fits allow us to trace the size of the emission region of the TDE to an unprecedented early phase, when it had a likely size corresponding to tens of gravitational radii. We are also able to trace the likely velocities based on the radius evolution, finding that it is either expanding at a rate well below the local escape speed or it is a very compact emission region at a much larger distance from the BH than its apparent size.

While no other TDE has a light curve that captures the rise to peak like the *TESS* light curve of ASASSN-19bt, some TDEs have been observed at 30–40 days prior to peak—notably, PS18kh (Holoien et al. 2019a; van Velzen et al. 2019) and ASASSN-18pg (Leloudas et al. 2019). It is unclear whether these other objects can be fit with the same power-law model that we use here to fit the rise of ASASSN-19bt, but it is possible that these and other future discoveries will have data close enough to first light to be able to constrain the power-law parameters. Using ASASSN-19bt as a guide, this likely requires data within the first ∼1–2 weeks after the light curve begins to rise in order to have enough data points to constrain the fit.

ASASSN-19bt is a poster child for a new era in early TDE studies. While not all TDEs will be found in the *TESS* CVZ, or be detected by *TESS* at all, TDEs are being found in greater numbers and at earlier times by surveys like ASAS-SN. This allows us to trigger multiwavelength follow-up observations earlier and probe the emission region at very early times. As more TDEs are found and observed extensively prior to peak, we will be able to build a better theoretical understanding of how the stellar debris evolves and how the accretion disk forms after disruption, hopefully illuminating the physics behind the later emission that we have been limited to studying for the majority of the TDEs found to date.

We thank the *Swift* PI, the Observation Duty Scientists, and the science planners for promptly approving and executing our *Swift* observations. We thank the *XMM-Newton* team for promptly scheduling and executing our TOO observations. We thank the Las Cumbres Observatory and its staff for its continuing support of the ASAS-SN project. This research utilizes Las Cumbres Observatory observations obtained with time allocated through the National Optical Astronomy Observatory TAC (NOAO Prop. ID 2018B-0110, PI: P. Vallely).

ASAS-SN is supported by the Gordon and Betty Moore Foundation through grant GBMF5490 to the Ohio State University and NSF grant AST-1515927. Development of ASAS-SN has been supported by NSF grant AST-0908816, the Mt. Cuba Astronomical Foundation, the Center for Cosmology and AstroParticle Physics at the Ohio State University, the Chinese Academy of Sciences South America Center for Astronomy (CASSACA), the Villum Foundation, and George Skestos.

P.J.V. is supported by the National Science Foundation Graduate Research Fellowship Program Under grant No. DGE-1343012. K.A.A. is supported by the Danish National Research Foundation (DNRF132). K.Z.S., C.S.K., and T.A.T. are supported by NSF grants AST-1515876, AST-1515927, and AST-1814440. C.S.K. is also supported by a fellowship from the Radcliffe Institute for Advanced Studies at Harvard University. K.D.F. is supported by Hubble Fellowship grant *HST*-HF2-51391.001-A, provided by NASA through a grant from the Space Telescope Science Institute, which is operated by the Association of Universities for Research in Astronomy, Incorporated, under NASA contract NAS5-26555. Support for J.L.P. is provided in part by FONDECYT through the grant 1191038 and by the Ministry of Economy, Development, and Tourism's Millennium Science Initiative through grant IC120009, awarded to The Millennium Institute of Astrophysics, MAS. S.D. acknowledges Project 11573003 supported by NSFC. T.A.T. acknowledges support from a Simons Foundation Fellowship and from an IBM Einstein Fellowship from the Institute for Advanced Study, Princeton. Support for this work was provided by NASA through Hubble Fellowship grant #51386.01 awarded to R.L.B. by the Space Telescope Science Institute, which is operated by the Association of Universities for Research in Astronomy, Inc., for NASA, under contract NAS 5-26555. J.S. acknowledges support from the Packard Foundation.

This paper includes data collected by the *TESS* mission, which are publicly available from the Mikulski Archive for Space Telescopes (MAST). Funding for the *TESS* mission is provided by NASA's Science Mission directorate.

This paper includes data gathered with the 6.5 m *Magellan* Telescopes located at Las Campanas Observatory, Chile.

Based on observations obtained at the Southern Astrophysical Research (SOAR) telescope, which is a joint project of the Ministério da Ciência, Tecnologia, Inovações e Comunicações (MCTIC) do Brasil, the U.S. National Optical Astronomy Observatory (NOAO), the University of North Carolina at Chapel Hill (UNC), and Michigan State University (MSU).

Software: FAST (Kriek et al. 2009), IRAF (Tody 1986, 1993), HEAsoft (Arnaud 1996), XSPEC (v12.9.1; Arnaud 1996).

ORCID iDs

Thomas W.-S. Holoien https://orcid.org/0000-0001-9206-3460
Katie Auchettl https://orcid.org/0000-0002-4449-9152
Christopher S. Kochanek https://orcid.org/0000-0001-6017-2961
K. Decker French https://orcid.org/0000-0002-4235-7337
Jose L. Prieto https://orcid.org/0000-0003-0943-0026
Benjamin J. Shappee https://orcid.org/0000-0003-4631-1149
Jonathan S. Brown https://orcid.org/0000-0002-1885-6419
Michael M. Fausnaugh https://orcid.org/0000-0002-9113-7162
Subo Dong https://orcid.org/0000-0002-1027-0990
Subhash Bose https://orcid.org/0000-0003-3529-3854
Rachael L. Beaton https://orcid.org/0000-0002-1691-8217
Konstantina Boutsia https://orcid.org/0000-0003-4432-5037
Laura Chomiuk https://orcid.org/0000-0002-8400-3705
Thomas Connor https://orcid.org/0000-0002-7898-7664
Nidia Morrell https://orcid.org/0000-0003-2535-3091
Andrew B. Newman https://orcid.org/0000-0001-7769-8660
Gwen C. Rudie https://orcid.org/0000-0002-8459-5413
Jay Strader https://orcid.org/0000-0002-1468-9668

References

Alard, C. 2000, A&AS, 144, 363
Alard, C., & Lupton, R. H. 1998, ApJ, 503, 325
Alatalo, K., Cales, S. L., Rich, J. A., et al. 2016, ApJS, 224, 38
Arcavi, I., Gal-Yam, A., Sullivan, M., et al. 2014, ApJ, 793, 38
Arnaud, K. A. 1996, in ASP Conf. Ser. 101, Astronomical Data Analysis Software and Systems V, ed. G. H. Jacoby & J. Barnes (San Fransisco, CA: ASP), 17
Auchettl, K., Guillochon, J., & Ramirez-Ruiz, E. 2017, ApJ, 838, 149
Auchettl, K., Ramirez-Ruiz, E., & Guillochon, J. 2018, ApJ, 852, 37
Baldwin, J. A., Phillips, M. M., & Terlevich, R. 1981, PASP, 93, 5
Bellm, E. C., Kulkarni, S. R., Graham, M. J., et al. 2019, PASP, 131, 018002
Blagorodnova, N., Gezari, S., Hung, T., et al. 2017, ApJ, 844, 46
Breeveld, A. A., Curran, P. A., Hoversten, E. A., et al. 2010, MNRAS, 406, 1687
Brown, J. S., Holoien, T. W.-S., Auchettl, K., et al. 2017, MNRAS, 466, 4904
Brown, J. S., Kochanek, C. S., Holoien, T. W.-S., et al. 2018, MNRAS, 473, 1130
Brown, J. S., Shappee, B. J., Holoien, T. W.-S., et al. 2016, MNRAS, 462, 3993
Brown, T. M., Baliber, N., Bianco, F. B., et al. 2013, PASP, 125, 1031
Bruzual, G., & Charlot, S. 2003, MNRAS, 344, 1000
Burrows, D. N., Hill, J. E., Nousek, J. A., et al. 2005, SSRv, 120, 165
Burrows, D. N., Kinnea, J. A., Ghisellini, G., et al. 2011, Natur, 476, 421
Cacella, P., Morrell, N., Vallely, P., et al. 2019, ATel, 12462, 1
Cardelli, J. A., Clayton, G. C., & Mathis, J. S. 1989, ApJ, 345, 245
Cenko, S. B., Bloom, J. S., Kulkarni, S. R., et al. 2012a, MNRAS, 420, 2684
Cenko, S. B., Krimm, H. A., Horesh, A., et al. 2012b, ApJ, 753, 77
Chornock, R., Berger, E., Gezari, S., et al. 2014, ApJ, 780, 44
Clemens, J. C., Crain, J. A., & Anderson, R. 2004, Proc. SPIE, 5492, 331
Dimitriadis, G., Foley, R. J., Rest, A., et al. 2019, ApJL, 870, L1
Dressler, A., Bigelow, B., Hare, T., et al. 2011, PASP, 123, 288
Evans, C. R., & Kochanek, C. S. 1989, ApJL, 346, L13
Fausnaugh, M. M., Vallely, P. J., Kochanek, C. S., et al. 2019, arXiv:1904.02171
French, K. D., Arcavi, I., & Zabludoff, A. 2016, ApJL, 818, L21
French, K. D., Yang, Y., Zabludoff, A. I., & Tremonti, C. A. 2018, ApJ, 862, 2
Garnavich, P. M., Tucker, B. E., Rest, A., et al. 2016, ApJ, 820, 23
Gaskell, C. M., & Rojas Lobos, P. A. 2014, MNRAS, 438, L36
Gehrels, N., Chincarini, G., Giommi, P., et al. 2004, ApJ, 611, 1005
Gezari, S., Cenko, S. B., & Arcavi, I. 2017, ApJL, 851, L47
Gezari, S., Chornock, R., Lawrence, A., et al. 2015, ApJL, 815, L5
Gezari, S., Chornock, R., Rest, A., et al. 2012, Natur, 485, 217
Guillochon, J., & Ramirez-Ruiz, E. 2013, ApJ, 767, 25
Hayasaki, K., Stone, N., & Loeb, A. 2013, MNRAS, 434, 909
Hayasaki, K., Stone, N., & Loeb, A. 2016, MNRAS, 461, 3760
Henden, A. A., Levine, S., Terrell, D., & Welch, D. L. 2015, AAS Meeting, 225, 336.16
Holoien, T. W.-S., Brown, J. S., Auchettl, K., et al. 2018, MNRAS, 480, 5689
Holoien, T. W.-S., Brown, J. S., Vallely, P. J., et al. 2019a, MNRAS, 484, 1899
Holoien, T. W.-S., Huber, M. E., Shappee, B. J., et al. 2019b, ApJ, 880, 120
Holoien, T. W.-S., Kochanek, C. S., Prieto, J. L., et al. 2016a, MNRAS, 463, 3813
Holoien, T. W.-S., Kochanek, C. S., Prieto, J. L., et al. 2016b, MNRAS, 455, 2918
Holoien, T. W.-S., Prieto, J. L., Bersier, D., et al. 2014, MNRAS, 445, 3263
Hung, T., Gezari, S., Blagorodnova, N., et al. 2017, ApJ, 842, 29
Jones, D. H., Read, M. A., Saunders, W., et al. 2009, MNRAS, 399, 683
Kalberla, P. M. W., Burton, W. B., Hartmann, D., et al. 2005, A&A, 440, 775
Kara, E., Dai, L., Reynolds, C. S., & Kallman, T. 2018, MNRAS, 474, 3593
Kauffmann, G., Heckman, T. M., Tremonti, C., et al. 2003, MNRAS, 346, 1055
Kelson, D. D., Williams, R. J., Dressler, A., et al. 2014, ApJ, 783, 110
Kewley, L. J., Dopita, M. A., Sutherland, R. S., Heisler, C. A., & Trevena, J. 2001, ApJ, 556, 121
Kochanek, C. S. 1994, ApJ, 422, 508
Kochanek, C. S. 2016, MNRAS, 461, 371
Kochanek, C. S., Shappee, B. J., Stanek, K. Z., et al. 2017, PASP, 129, 104502

Kriek, M., van Dokkum, P. G., Labbé, I., et al. 2009, ApJ, 700, 221
Lacy, J. H., Townes, C. H., & Hollenbach, D. J. 1982, ApJ, 262, 120
Law, N. M., Kulkarni, S. R., Dekany, R. G., et al. 2009, PASP, 121, 1395
Leloudas, G., Dai, L., Arcavi, I., et al. 2019, arXiv:1903.03120
Levan, A. J., Tanvir, N. R., Brown, G. C., et al. 2016, ApJ, 819, 51
MacLeod, C. L., Ivezić, Z., Sesar, B., et al. 2012, ApJ, 753, 106
Madigan, A.-M., Halle, A., Moody, M., et al. 2018, ApJ, 853, 141
McConnell, N. J., & Ma, C.-P. 2013, ApJ, 764, 184
Mockler, B., Guillochon, J., & Ramirez-Ruiz, E. 2019, ApJ, 872, 151
Moretti, A., Guzzo, L., Campana, S., et al. 2004, Proc. SPIE, 5165, 232
Nugent, P. E., Sullivan, M., Cenko, S. B., et al. 2011, Natur, 480, 344
Olling, R. P., Mushotzky, R., Shaya, E. J., et al. 2015, Natur, 521, 332
Peterson, B. M. 1993, PASP, 105, 247
Peterson, B. M., Ferrarese, L., Gilbert, K. M., et al. 2004, ApJ, 613, 682
Phinney, E. S. 1989, Natur, 340, 595
Piran, T., Svirski, G., Krolik, J., Cheng, R. M., & Shiokawa, H. 2015, ApJ, 806, 164
Poole, T. S., Breeveld, A. A., Page, M. J., et al. 2008, MNRAS, 383, 627
Rees, M. J. 1988, Natur, 333, 523
Remillard, R. A., & McClintock, J. E. 2006, ARA&A, 44, 49
Ricci, C., Trakhtenbrot, B., Koss, M. J., et al. 2017, ApJS, 233, 17
Rich, J. A., Kewley, L. J., & Dopita, M. A. 2015, ApJS, 221, 28
Ricker, G. R., Winn, J. N., Vanderspek, R., et al. 2015, JATIS, 1, 014003
Riess, A. G., Filippenko, A. V., Li, W., et al. 1999, AJ, 118, 2675
Roming, P. W. A., Kennedy, T. E., Mason, K. O., et al. 2005, SSR, 120, 95
Roth, N., & Kasen, D. 2018, ApJ, 855, 54
Roth, N., Kasen, D., Guillochon, J., & Ramirez-Ruiz, E. 2016, ApJ, 827, 3
Saxton, C. J., Soria, R., Wu, K., & Kuin, N. P. M. 2012, MNRAS, 422, 1625
Schlafly, E. F., & Finkbeiner, D. P. 2011, ApJ, 737, 103
Shappee, B. J., Holoien, T. W.-S., Drout, M. R., et al. 2019, ApJ, 870, 13
Shappee, B. J., Prieto, J. L., Grupe, D., et al. 2014, ApJ, 788, 48
Shiokawa, H., Krolik, J. H., Cheng, R. M., Piran, T., & Noble, S. C. 2015, ApJ, 804, 85
Stone, N. C., Generozov, A., Vasiliev, E., & Metzger, B. D. 2018, MNRAS, 480, 5060
Strauss, M. A., Weinberg, D. H., Lupton, R. H., et al. 2002, AJ, 124, 1810
Strubbe, L. E., & Murray, N. 2015, MNRAS, 454, 2321
Strubbe, L. E., & Quataert, E. 2009, MNRAS, 400, 2070
Sullivan, P. W., Winn, J. N., Berta-Thompson, Z. K., et al. 2015, ApJ, 809, 77
Tody, D. 1986, Proc. SPIE, 627, 733
Tody, D. 1993, in ASP Conf. Ser. 52, Astronomical Data Analysis Software and Systems II, ed. R. J. Hanisch, R. J. V. Brissenden, & J. Barnes (San Fransisco, CA: ASP), 173
Tonry, J. L., Denneau, L., Heinze, A. N., et al. 2018, PASP, 130, 064505
Vallely, P. J., Fausnaugh, M., Jha, S. W., et al. 2019, MNRAS, 487, 2372
van Velzen, S., Farrar, G. R., Gezari, S., et al. 2011, ApJ, 741, 73
van Velzen, S., Stone, N. C., Metzger, B. D., et al. 2019, ApJ, 872, 198
Vanderspek, R., Doty, J., Fausnaugh, M., et al. 2018, TESS Instrument Handbook (Cambridge, MA: MIT), https://archive.stsci.edu/files/live/sites/mast/files/home/missions-and-data/active-missions/tess/_documents/TESS_Instrument_Handbook_v0.1.pdf
Vinkó, J., Yuan, F., Quimby, R. M., et al. 2015, ApJ, 798, 12
Voges, W., Aschenbach, B., Boller, Th., et al. 1999, A&A, 349, 389
Wevers, T., Pasham, D. R., van Velzen, S., et al. 2019, MNRAS, 488, 4816
Wevers, T., van Velzen, S., Jonker, P. G., et al. 2017, MNRAS, 471, 1694
Wright, E. L., Eisenhardt, P. R. M., Mainzer, A. K., et al. 2010, AJ, 140, 1868